Rock-physics modelling of the North Sea greensand

Hossain, Zakir

Publication date:
2011

Document Version
Publisher's PDF, also known as Version of record

Technical University of Denmark

Rock-physics modelling of the North Sea greensand

Zakir Hossain

DTU Environment
Department of Environmental Engineering

PhD Thesis
May 2011

Rock-physics modelling of the North Sea greensand

Zakir Hossain

PhD Thesis
May 2011

DTU Environment
Department of Environmental Engineering
Technical University of Denmark

Zakir Hossain

Rock-physics modeling of the North Sea greensand

PhD Thesis, May 2011

The thesis will be available as a pdf-file for downloading from the homepage of the department: www.env.dtu.dk

Address:	DTU Environment Department of Environmental Engineering Technical University of Denmark Miljoevej, building 113 DK-2800 Kgs. Lyngby Denmark
Phone reception:	+45 4525 1600
Phone library:	+45 4525 1610
Fax:	+45 4593 2850
Homepage:	http://www.env.dtu.dk
E-mail:	reception@env.dtu.dk

Printed by:	Vester Kopi Virum, May 2011
Cover:	Torben Dolin
ISBN:	978-87-92654-36-6

Table of Contents

Preface

This PhD thesis entitled "Rock-physics modelling of the North Sea greensand" is based on three years research carried out at the Department of Environmental Engineering, Technical University of Denmark (DTU) with associate professor Ida Lykke Fabricius as the main supervisor. The project was financed by DTU and Dong A/E. Most of the experimental work for this thesis was carried out at DTU, GEO (Danish Geotechnical Institute) and GEUS (Geological Survey of Denmark and Greenland, co-operation with Niels Springer and Dan Olsen). Additional experimental work was carried out at Copenhagen University, Imperial College, London and University of Stavanger, Norway. During the PhD study I stayed around four months in the Stanford Reservoir Forecasting (SRF) group, Department of Energy Research Engineering, Stanford University, USA where I worked together with Associate Professor Tapan Mukerji.

The thesis consists of a synopsis and six papers. The papers include two published papers, one accepted paper, one submitted revised paper, one submitted paper and a peer reviewed conference paper.

Journal papers

I. **Hossain, Z.**, Fabricius, I.L., Grattoni, A. C. and Solymar, M. (2011): Petrophysical properties of greensand as predicted from NMR measurements. *Petroleum Geoscience,* vol 17, No. 2, pp 111-125.

II. **Hossain, Z.**, Fabricius, I.L., Mukerji, T. and Dvorkin, J. (2011): Rock Physics model of glauconitic greensand from the North Sea. *Geophysics* (submitted revised version).

In: SRB Annual Meeting 23-25 June, 2010. Stanford Rock Physics & Borehole Geophysics Project. Annual Report Vol. 121, p. B1-B21, Stanford University, Stanford, CA.

III. **Hossain, Z.**, Fabricius, I.L. and Mukerji, T. (2011): V_p-V_s relationship and AVO modelling for glauconite bearing sandstone. *Geophysical Prospecting* (in press).

IV. **Hossain, Z.** and Fabricius, I.L. (2011). Effect of CO_2 injection of physical properties of greensand. *Journal of Petroleum science and Engineering* (submitted).

Journal papers (related studies):

V. **Hossain, Z.**, and Mukerji, T (2011). Statistical rock physics and Monte Carlo simulation of seismic attributes for greensand (Accepted for EAGE annual meeting, Vienna, May 23-26, 2011).

VI. **Hossain, Z.**, Fabricius, I.L. and Christensen, H.F. (2009): Elastic and non-elastic deformation of greensand. *The Leading Edge*, Volume 28, Issue 1, pp. 86-88.

The papers are not included in this www-version, but can be obtained from the library at DTU Environment. Contact library@env.dtu.dk or Department of Environmental Engineering, Technical University of Denmark, Miljoevej, Building 113, DK-2000 Kgs. Lyngby, Denmark.

Acknowledgements

In 2005 I first came to DTU to pursue a Master of Science degree in Petroleum Engineering. I was supposed to go somewhere in the world after finishing my Master degree. However, I was so lucky that I found Associate Professor Ida Lykke Fabricius as my supervisor for my Master thesis. During my thesis Ida offered me for doing PhD in DTU. That was the greatest opportunity in my life so far. My last three years here at DTU have been a fantastic and rewarding experience. I would like to thank Ida Fabricius for being a fantastic advisor; she has guided me along the path that led to where I am today. Last three years with her help I completed not only a PhD thesis but also a wonderful scientific moment in my life.

I would like to thank Associate professor Tapan Mukerji, Stanford University. I had great time with him during my external research in Stanford. I feel very lucky that I was able to visit Stanford and could collaborate with Tapan during my research. I also would like to thank Gary Mavko and Jack Dvorkin, SRB research group, Stanford University. Special thanks to Jack for his collaboration with one of my papers. I also thank my friend Sadeem, Kaushik and Tanima (Exxonmobil) for their help during my stay in Stanford. I also thank Ida to send me Stanford University for my external research.

Furthermore, I want to thank all the people who were somehow involved with my PhD studies. Special thanks to Monzurul Alam for his help and support during my study. Thanks to Ahmed, Morten, Katherine Hedegaard, Katherine Andreassen, Ernest for all the great time I had together with them. I also like to thank all my co-authors for their great collaboration. Sinh Hy Nguyen is thanked for helping me during the lab work. I thank Hector Ampuero Diaz for making my thin sections. I thank Helle, Frederick, Morten, Igor from GEO for their help during the lab work throughout my studies. I thank Dan Olsen for carried out my CO_2 flooding experiment. Niels Spring and Hans Jørgen Lorentzen from GEUS are thanked for advises and help with laboratory work.

I would like to thank Dong E/A for their data, samples, and financial support for my PhD project.

At last but not all, I like to thank my wife Shila and my lovely young sweet daughter Zineta for their big support and understanding. I appreciate their patience and sacrifice during my PhD studies.

Kgs. Lyngby, Zakir Hossain
March 2011

Summary

Greensands are composed of a mixture of stiff clastic quartz grains and soft glauconite grains. Glauconites are porous and composed of aggregates of iron-bearing clay. Greensands from the two formations in the Nini field of the North Sea were studied in this thesis. Hermod Formation is weakly cemented, whereas Ty Formation is characterized by microcrystalline quartz cement. A series of laboratory experiments including core analysis, capillary pressure measurements, NMR T_2 measurements, acoustic velocity measurements, electrical properties measurements and CO_2 injection experiments were done on greensand samples. Thin sections and BSE images are also available for this study.

The objective of the first part of this study is to predict petrophysical properties from nuclear magnetic resonance (NMR) T_2 distributions. NMR is a useful tool in reservoir evaluation. Estimated petrophysical properties from NMR measurements were correlated with measurements from core analysis. NMR underestimates the total porosity due to the presence of iron bearing clay minerals in greensand. Permeability may be predicted from NMR by using Kozeny's equation when surface relaxivity is known. The surface area measured by the BET method is associated with the micro-porous glauconite grains. The effective specific surface area as calculated from Kozeny's equation is associated with macro-pores. Capillary pressure drainage curves may be predicted from NMR T_2 distribution when pore size distribution within a sample is homogeneous.

The central part of this study is rock-physics modelling of greensand. The first of the models is a grain contact model of the North Sea Paleocene greensand. First a Hertz-Mindlin contact model is developed for a mixture of quartz and glauconite. Next step is to use the moduli predicted from this Hertz-Mindlin contact model of two types of grains as the initial moduli for a soft-sand model and a stiff-sand model. Results of rock-physics modelling and thin section observations indicate that variations in the elastic properties of greensand can be explained by two main diagenetic phases: silica cementation and berthierine cementation. Initially greensand is a mixture of mainly quartz and glauconite; when weakly cemented, it has relatively low elastic modulus and can be modeled by a Hertz-Mindlin contact model of two types of grains. Silica-cemented greensand has a relatively high elastic modulus and can be modeled by an intermediate-stiff-sand or a stiff-

sand model. Berthierine cement has a different growth patterns in different part of the greensand, resulting in a soft-sand model and an intermediate-stiff-sand model.

The second rock-physical model predicts V_p-V_s relations and AVO of a greensand shale interface. The relationship between V_p and V_s may be used to predict V_s where only V_p is known. In published work, focus is primarily on the V_p-V_s relationship of quartzitic sandstone. In order to broaden the picture V_p-V_s relationships of greensand were presented. A V_p-V_s relationship derived from modelling is compared with empirical V_p-V_s regressions from laboratory data. The quality of V_s prediction is quantified by statistical analysis. The V_p-V_s relationship derived from modelling works well for greensand shear-wave velocity prediction. AVO modelling shows that brine saturated glauconitic greensand may have similar seismic response to oil saturated quartzitic sandstone and that strongly cemented greensand with oil saturation can have similar AVO response to brine saturated weakly cemented greensand.

The third rock-physical model predicts pore fluid effects on elastic properties of greensand. NMR studies were included to describe the fluid related dispersion in greensand. NMR studies show that Biot's flow should occur only in large pores in the greensand, while Biot's flow should not occur in micro-pores. Differences of fluid flow in macro-pores and micro-pores are described as high frequency squirt flow in greensand.

The objective of the last part of this study is to investigate CO_2 injection effects on physical properties of greensand. Laboratory results indicate that CO_2 injection has no major effect on porosity, electrical properties and elastic properties of greensand. In contrast Klinkenberg permeability of greensand increased after CO_2 injection. An NMR permeability modelling approach was tested to evaluate the effect on matrix permeability of CO_2 injection. It appears that permeability after CO_2 injection increased not due to fracturing but rather due to the increase of macro-pores in the greensand. The increase of macro-pores size is probably due to migration of fine pore-filling minerals. Rock-physics modelling indicates that the presence of CO_2 in a greensand decreases V_p by 2%-41% relative to V_p of brine saturated greensand. CO_2 flooding would at the same time increase V_s, typically 1%-2%, while decreasing density by 3%-5%.

Dansk sammenfatning

Grønsand består af en blanding af stive kvartskorn og blødere glaukonitkorn. Glaukonitkorn er porøse aggregater af jernholdigt ler. I denne ph.d.-afhandling undersøges grønsand fra to formationer i Nordsøens Nini felt. Hermod Formationen er kun svagt cementeret, mens Ty Formationen indeholder mikrokrystallin kvartscement. På kerneprøver fra de to formationer blev der foretaget laboratoriemålinger af bl.a. kapillartrykskurver, kernemagnetisk resonansspektrometri (NMR), hastighed af elastiske bølger (Vp og Vs), elektriske egenskaber samt effekten af CO_2-injektion. Tyndslibsbeskrivelser og elektronmikroskopbilleder var til rådighed.

I første del af afhandlingen undersøgtes anvendelsen af NMR til at forudsige reservoiregenskaber. Ved at sammenligne fysiske egenskaber målt direkte på kerneprøver med de samme egenskaber modelleret ud fra NMR vistes det, at NMR er et nyttigt redskab til reservoirkarakterisering. Porøsitet bestemt ud fra NMR er dog for lav, sandsynligvis på grund af glaukonits indhold af jern. Permeabilitet kan modelleres ret nøjagtigt ved en ny metode til anvendelsen af Kozenys ligning. Metoden kræver kendskab til mineralernes overfladerelaksering. Det ses, at den specifikke overfalde som målt med kvælstofadsorption (BET) domineres af bidrag fra de porøse glaukonitkorn, mens den effektive specifikke overflade beregnet ved hjælp af Kozenys ligning må associeres til makroporerne. For homogene prøver kan kapillartrykskurven modelleres ud fra NMR.

Afhandlingens centrale afsnit omhandler bjergartsfysisk modellering af grønsand. Først undersøgtes en kornkontaktsmodel af Hertz-Mindlin typen for blandinger af kvartskorn og glaukonitkorn svarende til det palæogene nordsøfelt. Denne kornkontaktmodel dannede basis for videre modellering ved hjælp af ”soft-sand” og ”stiff-sand” modeller. Resultaterne af den bjergartsfysiske modellering kombineret med observationer i tyndslib viste, at variationen i grønsandets elastiske egenskaber kan forklares ud fra to diagenetiske faser: kiselcementering og cementering med berthierin. I udgangspunktet er grønsand en blanding af kvartskorn og glaukonitkorn. Når det kun er svagt cementeret, har det lave elastiske moduli, som kornkontaktmodellen er tilstrækkelig til at modellere. Kiselcementeret grønsand har relativt høje elastiske moduli, som kan modelleres ved hjælp af ”intermediate-stiff-sand” og ”stiff-sand” modeller.

Berthierincementering giver anledning til elastiske moduli, der kan modelleres ved hjælp af ”soft-sand” eller ”intermediate-stiff-sand” modeller.

Dernæst undersøgtes modeller til at forudsige Vp-Vs relationer og til AVO analyse af en kontaktflade mellem lerskifer og grønsand. Vp-Vs relationer bruges til at forudsige Vs, når kun Vp kendes. Der findes allerede publicerede Vp-Vs relationer for kvartssand, mens grønsand er mindre velkendt. De bjergartsfysisk modellerede Vp-Vs relationer svarer inden for måleusikkerheden til direkte målte Vp-Vs relationer. AVO modellering viste, at vandmættet grønsand kan give samme seismiske respons som oliemættet kvartsand; samt at stærkt cementeret grønsand med olie kan give samme seismiske respons som vandmættet svagt cementeret grønsand.

Den tredje bjergartsfysike model af grønsand beskriver porevæskens indvirkning på de elastiske moduli. NMR data blev inddraget til at beskrive grønsand som en blanding af mikroporøse korn, der typisk vil være lavfrekvente i henhold til Biots model, og af korn og store porer, der kan beskrives som et højfrekvent system i henhold til Biot. Trykgradienter i porevæsken på grund af kontraster i porestørrelsen kan beskrives ved hjælp af en Squirt model.

Den sidste del af afhandlingen omhandler effekten af CO_2-injektion i vandmættet grønsand. Laboratoriemålingerne viste ingen tydelig effekt på porøsitet, elektriske egenskaber eller elastiske egenskaber af det vandmættede sand. Derimod iagttoges en forstørret permeabilitet. For at vise at denne effekt ikke bare skyldtes opsprækning, modelleredes permeabiliteten ud fra NMR data, og det vistes, at permabilitetsforøgelsen kan skyldes ændring i porestørrelsesfordelingen på grund af omfordeling af fine partikler. Den forventede seismiske respons på CO_2-injektion modelleredes. Vp forventes at ville mindskes med 2%-41%, Vs at ville øges med 1%-2%, mens massedensiteten vil mindskes med 3%-5%.

1. Introduction

Greensands are glauconite bearing sandstones. Greensand petroleum reservoirs can be found all over the world, e.g. the Mid-Cretaceous Safaniya Sandstone Member in Saudi Arabia (Cagatay et al., 1996), a Lower Cretaceous Glauconitic Sandstone in Alberta, Canada (Tilley and Longstaffe, 1984), the Upper Cretaceous Shannon Sandstone in Wyoming, USA (Ranganathan and Ty, 1986), a Lower Cretaceous Greensand offshore Ireland (Winn, 1994) and Late Paleocene Greensand in central part of the North Sea (Solymar, 2002; Solymar et al., 2003; Schiøler et al., 2007; Stokkendal et al., 2009; Hossain et al., 2009; Hossain et al., 2010a; Hossain et al., 2010b; Hossain et al., 2010c; Hossain et al., 2010d; Hossain et al., 2011a; Hossain et al., 2011b; Hossain et al., 2011c). Greensands are composed of a mixture of stiff clastic quartz grains and soft glauconite grains. Glauconites are also porous and composed of aggregates of iron-bearing clay (Figure 1.1). In fact, evaluation of greensand reservoirs has challenged geologists, engineers as well as petrophysicists. Diaz et al. (2003) found that the amount of glauconite in greensand has effect on porosity, permeability and elastic properties of reservoir rocks. Glauconite is also ductile (Ranganthan and Ty, 1986) therefore glauconites can cause non-elastic deformation (Hossain et al., 2009). Slot-Petersen et al. (1998) and Hamada et al. (2001) found that greensands show low resistivity in the reservoir zone due to the large amount of bound water in the glauconite. Furthermore, Rueslåtten et al. (1998a) described that paramagnetic glauconite or pore filling berthierine in greensand may induce magnetic gradients on the pore level causing the NMR T_2 relaxation time to be shortened dramatically.

The combination of conventional core analysis, such as Helium porosity, Gas permeability, specific surface area by BET and image analysis of thin section micrographs is effective in the evaluation of normal reservoir rocks. However, for glauconite bearing greensand where a high proportion of micro-porosity in glauconite grains creates an uncertainty with respect to fluid distribution and fluid saturation, an accurate determination of petrophysical properties by using conventional core analysis is difficult (Rueslåtten et al., 1998b). Therefore, NMR measurements may be used to quantify petrophysical properties of greensand. The objective of Nuclear Magnetic Resonance (NMR) measurements on reservoir core samples is to obtain an improved interpretation of logging data. NMR is a non-invasive technique that causes net magnetization of a hydrogen

atom (^{1}H) in the presence of an external magnetic field. NMR spectrometry involves a series of manipulations of the hydrogen proton found in pore fluids of a sedimentary rock. A measurement sequence starts with proton alignment to a magnetic field followed by spin tipping and decay. The quantities measured include signal amplitude which is proportional to the number of hydrogen nuclei and decay, also called relaxation time (Kenyon et al., 1995). The relaxation time is normally used to quantify porosity, permeability and the capillary pressure curve of a reservoir rock. The relaxation time may also be used to quantify the fluid flow within macro-pores and micro-pores in greensand.

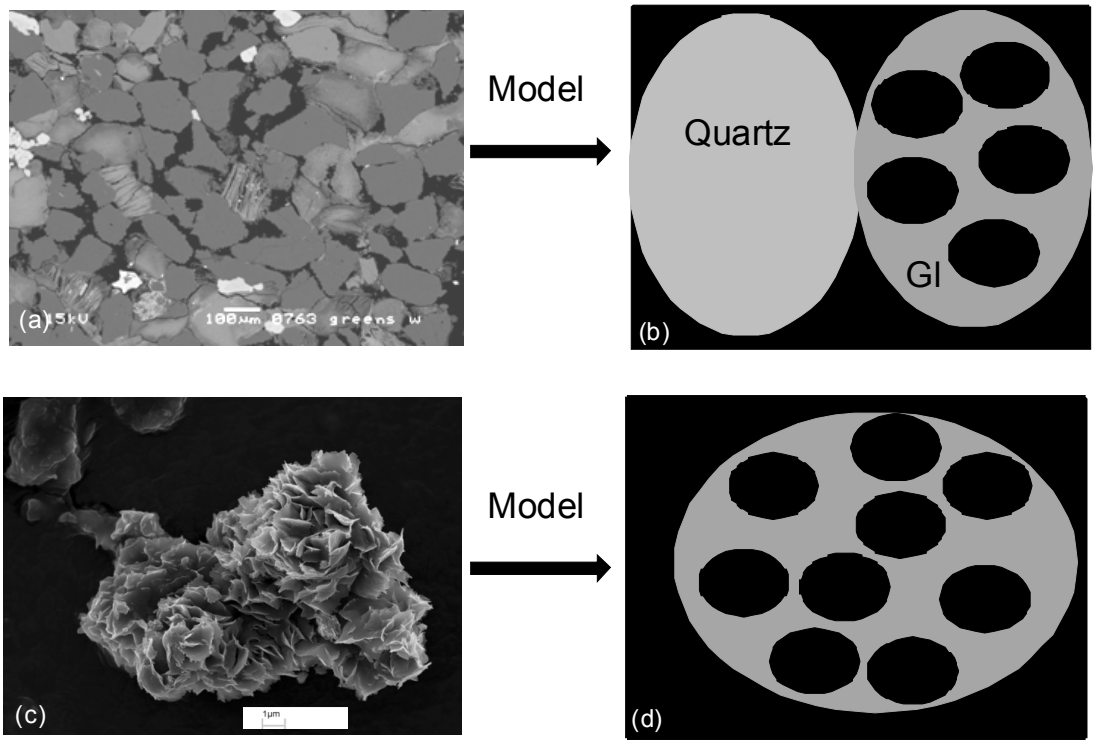

Figure 1.1. *(a) BSE image of the North Sea greensand and (b) its idealized model. (c) Glauconite grain from Arnager greensand (courtesy of Egil Nybakk) and (d) its idealized model. Scale bar for greensand is 100 μm and the image represents macro-porosity, quartz and glauconite grains. Scale bar for glauconite grain is 1 μm. Micro-pores reside within glauconite grain.*

Rock-physics modelling becomes an integral part of geophysics, petrophysics and geology. Rock-physics modelling bridges the elastic properties and geological properties. Rock-physics modelling has been used as a tool to 4D seismic monitoring of a reservoir, to discriminate seismic lithology and to detect hydrocarbon. In published work, laboratory ultrasonic measurements have been performed in quartz sandstone and shaly sandstone, and various theoretical

models have been developed (see overview in Mavko et al., 2009). However, rock-physics models for greensand are not well defined yet. Even though lots of rock-physics models are cited in the literature, their limitations and assumptions have always made it difficult to compare models to real rock properties. In order to make a rock-physics model universal, physical behavior of rocks should be honored. Hence an accurate estimation of physical properties can be a useful input for rock-physics modelling of greensand.

Granular media contact models are widely used rock-physics models for calculating the elastic properties of rocks. Contact models determine the elastic properties of granular media by deformability and stiffness of grain to grain contacts. Most of the contact models are developed based on the Hertz-Mindlin theory for the elastic behavior of two spheres in contact. However, for the sand-pack for sandstone, it is assumed that only quartz grains are packed together, and the normal and shear stiffness are calculated based on the contact of two quartz grains. For rocks with mixed mineralogy, a homogeneous mineral modulus is assumed. Then the normal and shear stiffnesses are calculated based on the contact of two average-mineralogy grains. Average-mineralogy is normally derived by using Hill's average. In fact, this is probably only applicable when the moduli of mixed minerals are quite comparable. This is probably not adequate when the elastic contrasts between mixed minerals are quite different. For greensands, the initial sand-pack is a mixture of quartz and glauconite, and because both of them are load bearing, elastic properties in between those of quartz and glauconite are anticipated. A Hertz-Mindlin contact model based on single grain type is not enough to estimate the elastic properties of mixtures of quartz and glauconite.

A part of rock-physics modelling is establishing V_p-V_s relationship and AVO analysis. A V_p-V_s relationship is normally used to predict V_s where only V_p is known. It is also used for AVO analysis and to identify the pore fluids from seismic data. Without V_s it is often difficult to separate the seismic signature according to lithology, pore fluids and pore pressure. In published work, focus is primarily on the V_p-V_s relationship and AVO analysis of quartzitic sandstone. However, the V_p-V_s relationship of greensand has not yet been defined. Furthermore, the elastic moduli of micro-porous glauconite grains and their effect on the V_p-V_s relationship are also unknown. AVO modelling is a step in multidisciplinary integration of petrophysics, rock physics, seismic data, geology

as well as petroleum engineering. One of the main objectives for AVO analysis is to predict the lithology and pore fluids from seismic data. However, in some cases AVO has been applied without success and the use of a too simple geological model is one of the reasons for failure. Therefore, the understanding of AVO response based on greensand properties is essential before using it for reservoir characterization.

Gassmann's fluid substitution method is widely used to predict velocities for saturated rock based on the velocities from dry rock. Gassmann's equations generally work at low frequency and do not take into consideration the fluid related dispersion. In some cases Biot's theory is used to describe the fluid related dispersion. In fact, several studies showed that Biot's theory does not fully explain the frequency dispersion for natural saturated rocks. By squirt relations, Mavko and Jizba (1991) show that water saturated rock may have larger velocity dispersion that would be predicted from Gassmann's equations and even prediction from Biot's high frequency case. Nevertheless, frequency related dispersion is not well studied for complex rocks as greensand. In the squirt flow mechanisms, the local flow in small cracks gives rise to local stiffening pressure gradients in the fluid. In greensand, it is possible that the contrast between flow in macro-pores and micro-pores within glauconites gives rise to a local stiffening pressure gradient in the fluid. Then fluid flow in greensand could then be described as squirt flow.

CO_2 capture and storage (CCS) is a technique to reduce CO_2 emission, and CO_2 is also used in EOR (enhanced oil recovery). It may increase oil production by 15%-25% from an oil field. CO_2 may be stored either as gas or dissolved in an aqueous solution in aquifers or in depleted oil or gas reservoirs. The consequence of CO_2 injection into a geological formation needs to be considered including the physical and chemical interaction of CO_2 with rock minerals and pore fluids. At reservoir conditions, CO_2 dissolved in water is in equilibrium with carbonic acid. The acid reacts with the rock thus changing its physical and mechanical properties. Even though CO_2 injection effect studies are common, they do not cover greensand reservoirs. The CO_2 injection processes in greensand could be more complicated than in quartz sand, because, interaction of CO_2 with glauconite is expected rather than with quartz. Furthermore, greensand from the North Sea contains micro-crystalline quartz and pore-filling clay (berthierine)

cement (Solymar et al., 2002; Hossain et al., 2011b). Moreover, in the case of Nini field a question is whether injected CO_2 can be detected seismically.

1.1 Scope of study

The title of the present PhD research project is rock-physics modelling of the North Sea greensand. This study was divided into several parts. The first part was related to the use of NMR to predict petrophysical properties of greensand. The central part of this study is concerned with rock-physics modelling of greensand including a contact model, an empirical model, AVO analysis, and fluid related dispersion analysis. The last part of this study addresses CO_2 injection effect on physical properties of greensand.

In the first part of this study related to predicting petrophysical properties from NMR T_2 distributions. Estimates of porosity, permeability, irreducible water saturation derived from NMR measurement were correlated with data from core analysis. The potential use of surface area data is also described and illustrated. Kozeny's equation was used for NMR permeability prediction. Furthermore P_c curves were estimated from NMR measurements and compared with laboratory results.

The central part of this study is concerned with rock-physics modelling of greensand. Effective medium models were applied to model the porous grain of glauconite. In greensands, the initial sand-pack is a mixture of quartz and glauconite, and because both of them are load bearing, elastic properties between those of quartz and glauconite are anticipated; a Hertz-Mindlin contact model for mixtures of quartz and glauconite was presented in this study. Then this Hertz-Mindlin contact model of two types of grains was used as initial modulus for a soft-sand model and a stiff-sand model. Using these rock-physics models, the effect of microstructure on the elastic properties of greensand was explored and finally the rock-physical properties were linked to greensand diagenesis by results from thin section analysis.

The second part of the rock-modelling addresses empirical V_p-V_s relationships and AVO modelling of greensand. The objectives of this study are to predict the velocity of the elastic shear wave (V_s) from velocity of the elastic compressional wave (V_p) and to investigate the AVO response of greensand. The effective medium based Iso-frame model was used to derive a V_p-V_s relationship for

greensand. Empirical V_p-V_s relationship for greensand was also derived from laboratory measured data. Widely used V_p-V_s relationships in literature are also used to predict V_s for giving a V_p. Statistical analysis was done to compare the predictions by using different relations. AVO modelling of glauconitic greensands was also done with the goal of better understanding AVO behavior for this kind of rock.

The third part of rock-physics modelling is concerned with pore fluid effects on elastic properties of greensand. The widely used Gassmann fluid substitution model was used to predict saturated moduli of greensand from dry moduli. Biot's critical frequency and NMR T_2 were combined to describe the differences in fluid flow within macro-pores and within micro-pores. Differences in fluid flow from micro-pores to macro-pores were described by a squirt model.

The last part of this study is related to CO_2 injection effects on physical properties of greensand. A CO_2 experiment on greensand samples was carried out to detect the CO_2 injection effect on physical properties. Petrophysical properties, elastic properties and electrical properties were compared before and after CO_2 injection. An NMR permeability modelling approach was used to evaluate the effect on matrix permeability of CO_2 injection. Furthermore, rock physics-based models were used to predict the changes of seismic properties due to the CO_2.

1.2 Geological and data setting for the Nini 1 field

The Nini field is located in Siri Canyon. Siri Canyon is part of a large system of submarine canyons in the Paleocene in the Norwegian-Danish Basin (Stokkendal et al., 2009). The reservoir consists of sand deposited in the Siri Fairway (Schiøler et al., 2007). The glauconite bearing sandstone in the Nini field is formally included in the Hermod Formation and in the older Ty Formation. These Paleocene reservoir sands are characterized by glauconite rich (20-30 vol %) fine grained and well sorted sand. In greensand both quartz grains and glauconite pellets are part of the load-bearing matrix. The greensand beds occur in a shale-sequence. In the Nini wells, the Hermod sand was found to be more massive, more porous and more permeable than Ty sand (Schiøler et al., 2007).

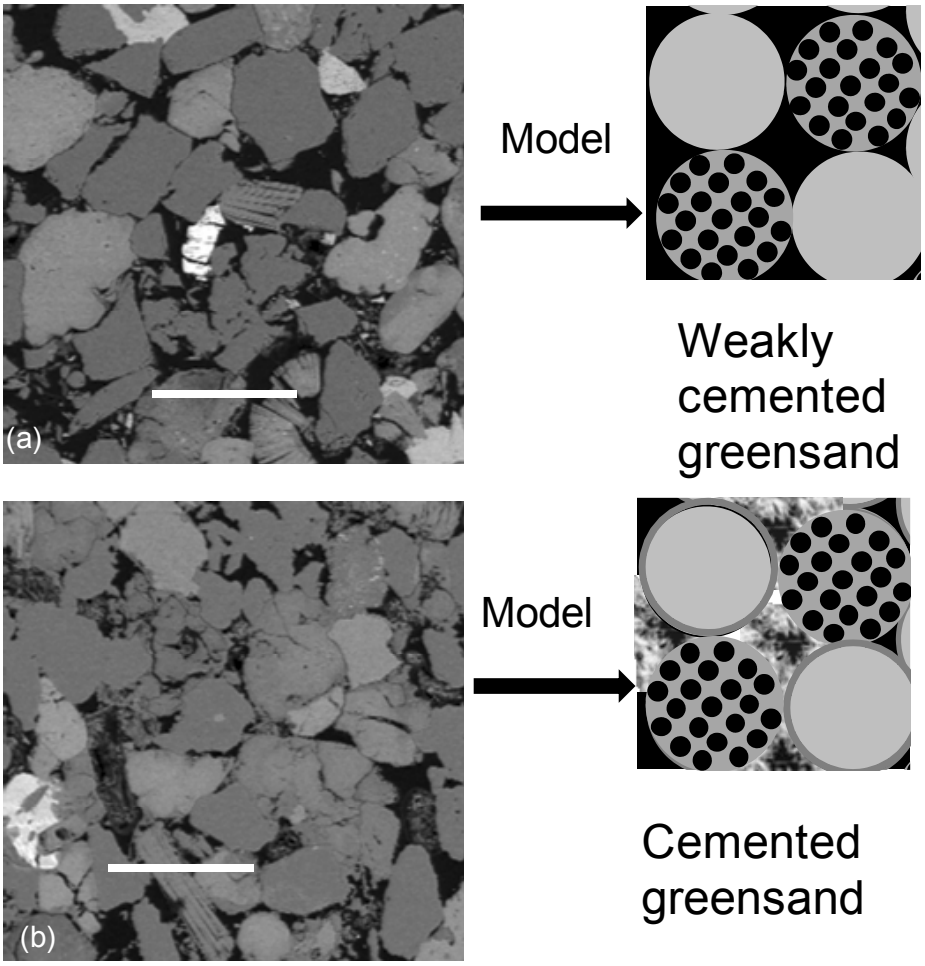

Figure 1.2. *BSE images of two types of greensands. Scale bar is 200μm. (a) Weakly cemented greensand and its idealized model and (b) cemented greensand and its idealized model.*

Solymar (2002) performed the petrographic thin section analysis of the studied greensand samples. Thin section analysis indicates that the studied Paleocene greensand are well to very well sorted, dominated by quartz but also large volume of glauconite (20-25 vol%). A smaller amount of feldspar, mica, as well as pore filling and pore lining minerals are also present in the studied greensand samples. Samples from Hermod Formation contain glauconite grains of size between 100 and 200 μm, some glauconite grains are larger (300 to 400 μm). Samples from Ty Formation contain glauconite grains of size between 100 and 150 μm, although some glauconite grains are larger (200 to 300 μm). The grains are sub-angular to sub-rounded in both Formations. However, the main difference between these two formations is that Hermod Formation is only weakly cemented, whereas samples from Ty Formation contain berthierine or microcrystalline quartz cement (Figure 1.2).

A series of log data including compressional wave velocity, shear wave velocity, density, gamma ray and resistivity from Nini 1 are available for this study. Sixteen one-and-half inch horizontal core plugs from the two greensand formations of the Nini field are included in this study. The samples have already been used for routine core analysis and were chosen to cover the range of variation in porosity (25%-40%) and air permeability (60 mD-1000 mD). All cores were cleaned of brine and hydrocarbons by soxhlet extraction with methanol and toluene prior to analysis. Thin sections were prepared from the end of each plug. Backscattered Electron Micrographs (BSE) from thin sections (courtesy of Mikael Solymar) are also available for this study. A series of laboratory experiments were performed on the greensand samples. Methods of petrophysical properties measurements including porosity, permeability, specific surface area, NMR and capillary pressure curves are described in Paper I. Methods of measuring elastic properties dry and brine saturation condition are described in Paper III. CO_2 injection methods on greensand samples are described in Paper IV. Methods of electrical properties measurement are described in Paper IV.

2. Petrophysical properties of greensand

2.1 NMR studies

NMR studies are widely used for characterization of petrophysical properties (e.g. Kenyon, 1997; Al-Mahrooqi et al., 2003; Al-Mahrooqi et al., 2006). Longitudinal relaxation time (T_1) measures the decay of spin alignment; transverse relaxation time (T_2) measures the decay of precession. Although T_1 measurements are more common in the literature, they are more time consuming than T_2 measurements. Hence, pulsed NMR logging tools preferentially measure T_2 for faster logging speeds (Straley et al., 1997). NMR transverse relaxation (T_2) of fluids confined in a porous rock is affected by pore surface, by the bulk relaxation process in the fluid and additionally by dephasing in case of molecular diffusion. T_2 may be expressed by the fundamental equation governing the NMR relaxation spectrum (Coates et al., 1999):

$$\frac{1}{T_2} = \frac{1}{T_{2Surface}} + \frac{1}{T_{2Bulk}} + \frac{1}{T_{2Diffusion}}. \qquad (2.1)$$

In the above equation, $T_{2Surface}$ is the surface relaxation which is the dominating mechanism in porous media, controlled by pore surface area. The relation between NMR relaxation and pore surface area results from strong interaction between the protons and the surface because the surface relaxivity (ρ) causes rapid alignment of hydrogen protons on the pore wall, while protons in the remaining fluid decay through itself (bulk relaxation, T_{2Bulk}), which is much slower (Howard et al., 1993). Bulk relaxation is thus significantly smaller than the surface relaxation and so where relation of diffusion ($T_{2Diffusion}$) is slow, the transverse relaxation (T_2) may be related to surface to volume ratio of pores (Sp) and surface relaxivity:

$$\frac{1}{T_2} = \rho_2 S_P. \qquad (2.2)$$

The NMR T_2 distributions of sixteen greensand samples are presented in graphical form and the populations are expressed in porosity units (p.u.) (Figure 2.1). All greensands have bimodal distribution. Each T_2 time corresponds to a particular pore size therefore, broader distribution reflect greater variability in pore size. The T_2 cutoff of 5.2 ms for the sample from Hermod Formation and

3.7 ms for the sample from Ty Formation was determined in the laboratory (details in Paper I). Therefore, in greensand samples a peak close to 1 ms should correspond to glauconite water, whereas all samples also present a second peak close to 100 ms that corresponds to movable fluid. Higher permeability greensands from Hermod Formation show larger amplitude in the movable fluid than samples from Ty Formations, whereas lower permeability samples from Ty Formation shows slightly larger amplitude in capillary bound glauconite water (Figure 2.1).

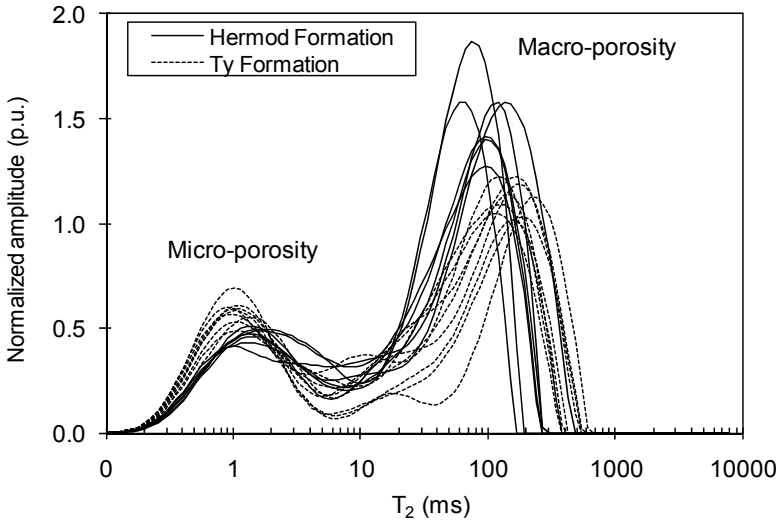

Figure 2.1. *NMR T_2 distribution curves shows two peaks for all greensand samples. The peaks close 1 ms represent micro-porosity and the peaks close to 100 ms represents macro-porosity.*

2.2 Porosity

Porosity is the key and primary parameter to evaluate the amount of hydrocarbon in a reservoir. NMR could be used as an effective tool to measure the formation porosity. However, several factors need to be considered before using an NMR tool in the greensand reservoir. Significant differences between NMR measured porosity and core analysis porosity was reported by several authors. Factors influencing the NMR T_2 measurements include paramagnetic minerals in the reservoir rock which may cause diffusion relaxation and hence reduce the T_2 relaxation time (Xie et al., 2008). They may also affect the surface relaxivity and produce a shift of the relaxation distribution to shorter time (Dodge et al., 1995).

Porosity of greensand ranges from 28 to 42 p.u. with a maximum uncertainty 1.5 p.u. However, laboratory measured Helium porosity, Archimedes porosity and NMR porosity are not equal (Figure 2.2). Helium porosity represents the total

porosity of greensand including micro-porosity within glauconite and it shows the highest values among the three types of porosity data. In principle Archimedes porosity and NMR porosity should also represent the total porosity in greensand unless the saturation is below 100%. Although the Archimedes porosity is close to Helium porosity, NMR porosity tends to be the lowest. Both Archimedes and NMR porosity were measured assuming that samples are 100% saturated. Therefore, the discrepancy between Archimedes porosity and NMR porosity could be due to the some factor that has influence on one of the measurement techniques. Paramagnetic iron-bearing minerals in reservoir rock may be an important factor influencing T_2 measurements as shown by Dodge et al. (1995). Paramagnetic iron-bearing minerals have no effect on Archimedes porosity measurements. The presence of paramagnetic ions increases the rate of relaxation of the hydrogen proton. This is expected for greensand because glauconite and berthierine are iron-bearing. These clay minerals have large surface area and high magnetic susceptibilities leading to large internal gradients and short T_2 (Straley et al., 1997). Rueslåtten et al. (1998a) studied NMR of iron-rich sandstone from the North Sea and illustrated the influence of chlorite (berthierine) and glauconite on the difference between Helium porosity and NMR T_2 derived porosity (delta porosity) and found broad positive correlation between delta porosity and chlorite content, whereas they found no correlation with glauconite content. Thus they pointed to the detrimental effect of chlorite or berthierine on NMR estimated porosity.

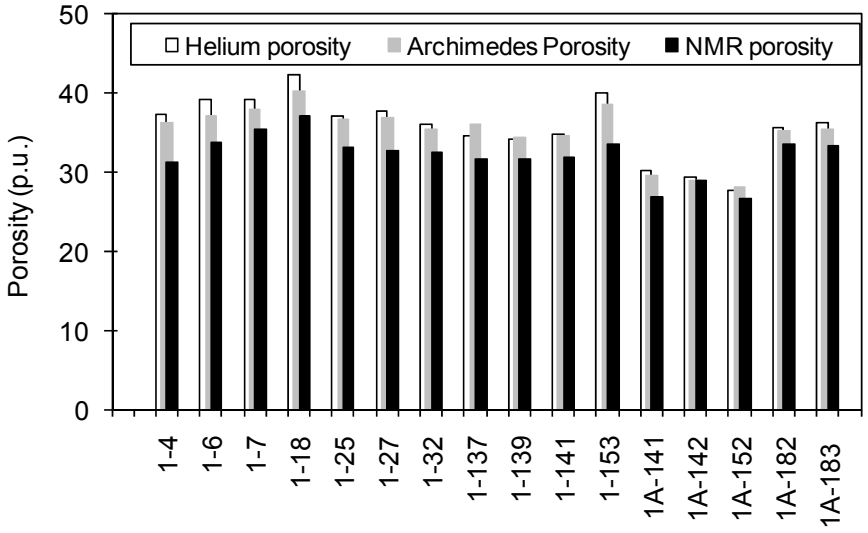

Figure 2.2. *Helium porosity, Archimedes porosity and NMR measured porosity of sixteen greensand samples. Helium porosity tends to be the highest, whereas porosity is underestimated by NMR measurements due to the iron bearing minerals in greensand.*

2.4 Permeability

Permeability is essential for reservoir characterization but can only be measured in the laboratory. Laboratory measured permeability provide the absolute permeability at core scale which could be different from formation permeability. NMR is the only tool that attempts to estimate *in-situ* formation permeability (Hidajat et al., 2002; Glover et al., 2006). Timur-Coates formula (Coates et al., 1999) is one of the most popular NMR derived permeability correlations used to calculate the formation permeability:

$$k_{NMR} = (C\phi)^m \left(\frac{FFI}{BFI}\right)^n, \tag{2.3}$$

where, ϕ is the porosity, *FFI* is the free fluid volume and *BFI* is the bound irreducible fluid, as determined from NMR T_2 distributions. Formation dependent constants *C*, *m* and *n* may be assumed to be 10, 4 and 2 for sandstones respectively, where NMR permeability, k_{NMR} is given in mD. This equation is just an empirical derived relationship that links various NMR-derived parameters to permeability and the complicated pore structure may not be described by the model. Therefore, predicted permeability by using this relationship may be unrealistic unless empirically calibrated parameters are used. In most cases these empirical parameters have no physical meaning and thus are only valid for special facies types and for local investigation. Kozeny's equation (Kozeny, 1927) is probably the most widely used physical permeability model. The Kozeny's equation may be implemented as (Kozeny, 1927; Mortensen et al. 1998):

$$k = c\frac{\phi^3}{S^2}, \tag{2.4}$$

where, *S* is the effective specific surface area, ϕ is the effective porosity and c is Kozeny's factor which can be estimated from the porosity via a simples model of 3D interpenetrating tubes (Mortensen et al., 1998):

$$c = \left[4\cos\left\{\frac{1}{3}\arccos\left(\phi\frac{8^2}{\pi^2}-1\right)+\frac{4}{3}\pi\right\}+4\right]^{-1}. \tag{2.5}$$

Specific surface of pores (*Sp*) can then be calculated as:

$$Sp = \frac{S}{\phi}. \tag{2.6}$$

Comparing Timur-Coates formula with Kozeny's equation indicates that porosity or pore volume strongly controls the permeability together with effective specific surface area as expressed by *FFI/BFI*. For homogenous sediments like chalk where the effective surface is equivalent to the one measured by nitrogen adsorption (BET), Kozeny's equation works well without introducing empirical factors (Mortensen et al., 1998). For less homogenous sediments like greensand, where effective surface is equivalent to the one measured by image analysis, Kozeny's equation works well to estimate permeability without introducing any empirical factors (Solymar, 2002). Kozeny's equation may be extended to calculate permeability from NMR T_2 distribution. By combining equation (2.2), (2.4), and (2.6) the permeability model for NMR measurements may be written as:

$$k = c\phi(T_2\rho_2)^2. \tag{2.7}$$

Equation (2.7) may be rewritten by summing the total permeability among the T_2 distribution accordingly:

$$k = c\phi\rho_2^2 \sum_{i=1}^{N} f_i (T_{2i})^2, \tag{2.8}$$

where, *fi* is a fraction of the total amplitude of each T_{2i}. The Kozeny factor, *c* is calculated by using equation (2.5).

The T_2 distribution of sample 1-18 peaks at longer time than for sample 1-6, thus the larger porosity of sample 1-18 is due to the larger pores which also cause higher permeability (Figure 2.2a). Predicted permeability distribution obtain by using equation (2.8) is shown in Figure 2.2b. Below 5.2 ms, the amplitude of permeability is close to zero which means micro-porosity within glauconite does not contribute significantly to fluid flow. Form 5.2 ms to 100 ms, the amplitude of permeability is small but above 100 ms the contribution permeability increases.

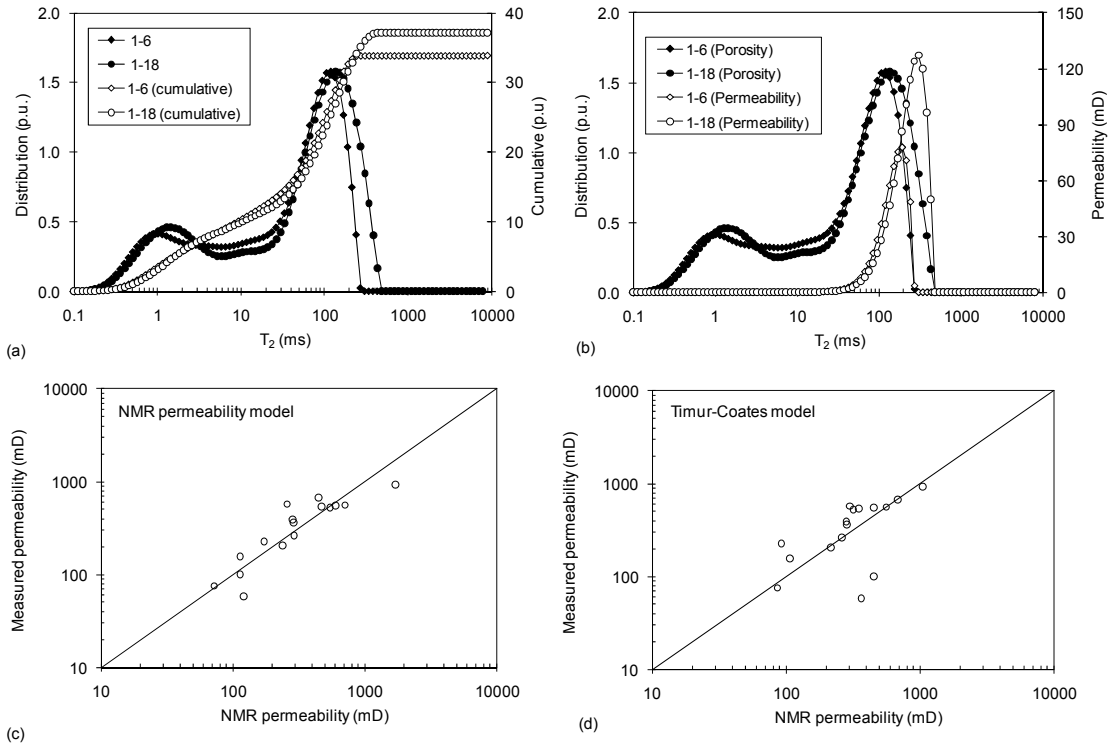

Figure 2.3. *(a) Porosity distribution and cumulative porosity of two greensand samples. (b) Porosity and permeability distribution of two greensand samples. (c) Klinkenberg permeability versus NMR predicted permeability by using Kozeny's (Kozeny 1927) equation. (d) Klinkenberg permeability versus NMR predicted permeability from Timur-Coates model.*

Predicted permeability by using equation 2.8 agrees well with measured permeability (Figure 2.2c). Predicted permeability by using Timur-Coates model works rather well if a formation dependent constant, C=8.3 is used which was optimized in a least-squares sense such that the sum of the squared error between the measured and predicted permeability is minimized.

2.5 Specific surface area

Specific surface area is a significant petrophysical parameter to understand the physics of porous media and to predict permeability. Specific surface area is related with porosity and permeability (Kozeny, 1927; Borre et al., 1997; Mortensen et al., 1998), with the fundamental equation governing the NMR relaxation spectrum (Coates et al., 1999), with capillary entry pressure (Røgen et al., 2002), with irreducible water saturation (Hamada et al., 1999; Hamada et al., 2001), with relative permeability (Morgan and Gordon, 1970), with Biot's critical frequency (Fabricius et al., 2010) and with cementation factor (Olsen et al., 2008). Riepe (1998) described that specific surface area never fully incorporated into special core analysis programs due to lack of petrophysical

understanding and concepts for correct evaluation. Nitrogen adsorption methods (BET) yield high specific surface value as nitrogen enters the pores in the sample. By using image analysis to determine the specific surface area, usually a much smaller value is derived, and the value depends upon the resolution (Solymar et al., 2003). Therefore, by using a high resolution BET surface or a highly smoothed surface derived from image analysis, the calculated permeability can be varied several orders of magnitude (Riepe, 1998). Thus specific surface measured by different methods reflects the pore properties at different scales.

The relationship between macro-porosity and permeability are correlated with specific surface area of pores determined from Kozeny's equation (Figure 2.4a). Therefore, specific surface area estimated from Kozeny's equation is associated with effective surface area and related to macro-porosity. Nitrogen adsorption has a very high resolution; therefore this method determines the specific surface of the total porosity, including micro-porosity. The specific surface area of separated glauconite grains are in order of 1300-1600 μm^{-1} (Solymar, 2002), whereas the specific surface area of quartz grains is less than 1 μm^{-1}. So rather than of quartz grains, it is the specific surface of glauconite grains which are measured by BET method. For a few samples relations between micro-porosity and permeability within micro-porosity are correlated with specific surface area of pores determined by the BET method (Figure 2.4b). Correlations were calculated by using Kozeny's equation where permeability within micro-pores was quantified from NMR T_2 distribution. Still most of the samples have higher permeability within micro-pores than that can be predicted from specific surface area by BET method. A higher specific surface area by the BET method is reflected in pore filling/lining clays. Thus, specific surface area by the BET method is reflected not only by the micro-pores of glauconite grains but also by pore filling/lining clays.

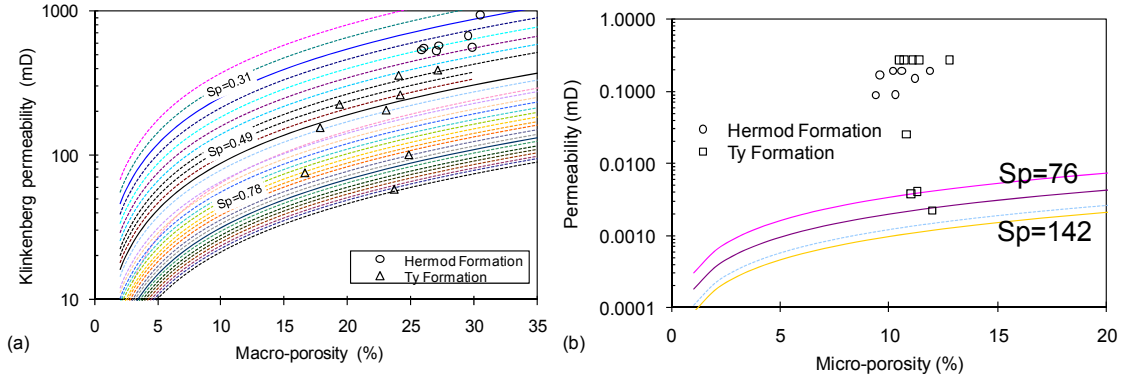

Figure 2.4. *(a) Relationship between macro-porosity and permeability. The reference lines represent the specific surface area of pores determined from Kozeny's equation. (b) Relationship between micro-porosity and permeability within micro-pores determined from NMR T_2 distribution. The reference lines represent the specific surface area of pores determined from BET method. Sample from Hermod Formation have similar porosity and permeability, whereas the samples from Ty Formation are more scattered.*

2.6 Capillary pressure curves

Capillary pressure curve (P_c) can be determined only from laboratory core analysis. However, several authors (e.g. Kleinberg, 1996, Grattoni et al., 2003, Marshal et al., 1995 and Volokitin et al., 1999) have also focused on the relationship between T_2 distribution and P_c curves and their general conclusion is that if the bulk relaxation and diffusion effect are ignored, a simple relation between T_2 and becomes:

$$P_c = \frac{K}{T_2}, \tag{2.9}$$

where, K is an empirical scaling factor introduced to predict capillary pressure curves. NMR derived P_c curves could be a fast, cheap and non-destructive estimation procedures. However the match between laboratory measured P_c curves and NMR derived P_c curves is not universal (e.g. Kleinberg, 1996). Equation (2.9) reflects that both the T_2 distribution and P_c curves are affected by pore structures but overlooks the difference between the physics of the processes. In a pore size and hydraulic radius model, P_c is sensitive to the hydraulic radius, whereas the NMR measures the pore body size (Kewan and Ning, 2008).

Laboratory measured capillary pressure curves show that for the higher permeability Hermod Formation samples, the Pc curves have lower irreducible

water saturation, whereas Pc curves for the low permeability Ty Formation samples have higher irreducible water saturation (Figure 2.5). Irreducible water saturation of greensand samples was obtained from capillary pressure at 100 psi, and varied between 25% and 42%.

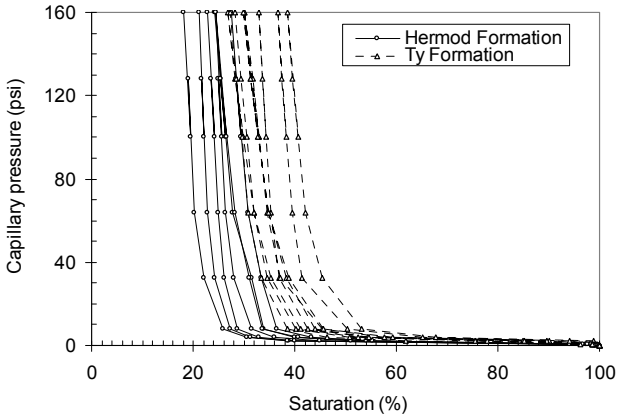

Figure 2.5. *(a) Capillary pressure curves of greensand samples. Capillary pressure curves of Hermod Formation samples have lower irreducible water saturation, whereas samples from Ty Formation have relatively higher irreducible water saturation. This pattern compares to the relatively lower permeability of Ty sand to the higher permeability of Hermod sand.*

Laboratory measured P_c and NMR derived P_c overlay each other for low permeability samples from the Ty Formation (Figure 2.6). However, the deviation between two types of P_c curves can be observed for the high permeability samples from the Hermod Formation. A deviation is to be expected, because the assumption of this model was that: 1- the pore structure controlling the T_2 distribution and capillary pressure is a bundle of capillary tubes and the drainage is controlled by the hierarchy of pore sizes; 2- the surface relaxivity is constant overall the sample; 3-diffusion relaxation is negligible. A good match between P_c curves from laboratory and NMR measurement is found when average surface relaxivity is equal to surface relaxivity applied to predict P_c curves from NMR. In contrast, a deviation between P_c curves from laboratory and NMR measurements is found when average surface relaxivity is not equal to the surface relaxivity need to match Pc curves. This variation of surface relaxivity within the sample is probably due to the large pores and higher permeability in the greensands of Hermod Formation.

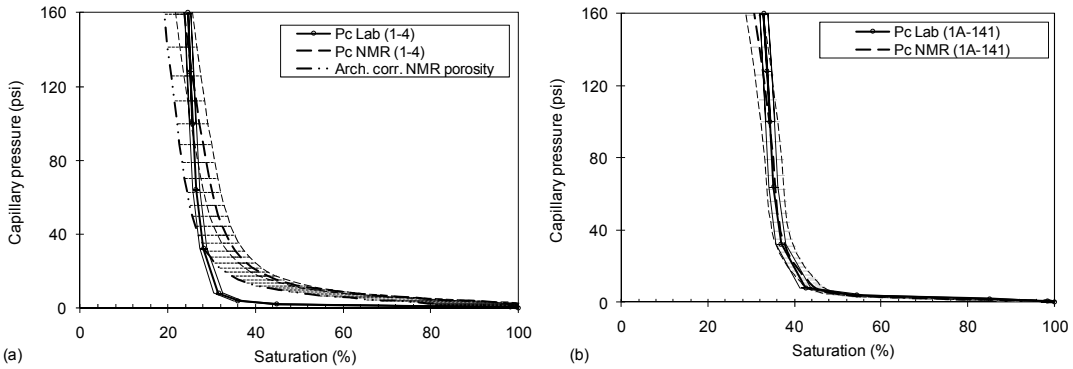

Figure 2.6. *Air brine capillary pressure curves including saturation error compared with NMR derived capillary pressure including saturation error (a) samples from Hermod formation and (b) sample from Ty formation.*

3. Rock-physics modelling of greensand

3.1 Rock-physics models

Rock-physics models in the literature can be divided into effective elastic medium or bound and mixing laws, granular media, fluid effect on wave propagation and empirical models. Effective elastic medium models include Hashin and Shtrikman bounds (Hashin and Shtrikman, 1963), Voigt and Reuss bounds (Voigt, 1910; Reuss, 1929), Hill average (Hill, 1952), Kuster and Toksöz formulation (Kuster and Toksöz, 1974; Berryman, 1980), the self-consistent approximation (Budiansky, 1965; Berryman, 1980), Differential effective medium model (Zimmerman, 1991; Mukerji et al.,1995), pore elastic Backus average (Backus, 1962); BAM model (Marion, 1990) and Iso-frame model (Fabricius, 2003; Fabricius et al., 2007). Granular-medium rock-physics models include the Hertz-Mindlin contact model (Hertz, 1882; Mindlin 1949); the Walton model (Watlon 1987); Digby's model (Digby 1981); The model of Jenkins (Jenkins et al., 2005); the model of Johnson (Norris and Johnson, 1997); the cemented-sand model (Dvorkin and Nur, 1996); the soft-sand model (Dvorkin and Nur, 1996); the stiff-sand and intermediate stiff-sand models (Mavko et al., 2009). Some of the existing granular medium models are summarized by Wang and Nur (1992). Biot's velocity relations (Biot, 1956a; Biot, 1956b), Gassmann's equations, (1951) and the squirt model (Mavko and Jizba, 1991) are mainly used to study the effect of fluid on wave propagations. In fact several models e.g. BISQ model (Dvorkin et al., 1994) and Iso-frame model (Fabricius, 2003) are also used to study the fluid effect on wave propagation. The most used empirical relations in the literature are Wyllie's time-average equation (Wyllie et al., 1956; Wyllie et al., 1958; Wyllie et al., 1962; Wyllie et al., 1963), Raymer-Hunt-Gardner relations (Raymer et al., 1980), Han's empirical relations (Han, 1986a) and Castagna's empirical relations (Castagna, 1985). Furthermore, amplitude variation with offset (AVO) by Zoeppritz's (Aki and Richards, 1984) and by Shuey (Shuey, 1985), elastic impedances (Connolly, 1999; Mukerji et al., 2001) as well as viscoelastic and attenuation are also part of rock-physics modelling.

In this thesis effective medium models were used for modelling of porous glauconite and also to describe the elastic contrast between quartz and glauconite. The Hertz-Mindlin contact model was modified for mixture of quartz and glauconite grains. The soft-sand model, stiff-sand model and intermediate stiff-

sand models were used to describe the diagensis of the North Sea greensand. The effective medium based Iso-frame model was used to derive a V_p-V_s relationship for greensand. Empirical V_p-V_s relations of Castagna's and Han's were used to predict V_s from V_p. Zoeppritz's equations and Aki and Richards approximations were used for AVO modelling of greensand. Biot's, Gassmann's and squirt models were used to describe pore fluid effects on greensand. Furthermore, Gassmann's equations were also used to describe the CO_2 injection effect on greensand.

3.2 Modelling of a porous glauconite grain

The simplest effective medium models are Reuss and Voigt bounds. The Reuss bound is the harmonic average of the elastic moduli of individual components of a composite, while the Voigt bound is the arithmetic average. The Hashin-Shtrikman bounds (Hashin and Shtrikman 1963) describe the narrowest possible range for an isotropic, linear elastic composite, when only the volume fractions are known. Tighter bounds exist when spatial correlations are known. The Hashin-Shtrikman bounds give the upper and lower limits of the data distribution for bulk and shear moduli as a function of the volume fractions of mixing materials. These bounds are narrower than those defined by the Reuss lower bound and the Voigt upper bound (Mavko *et al*. 2009).

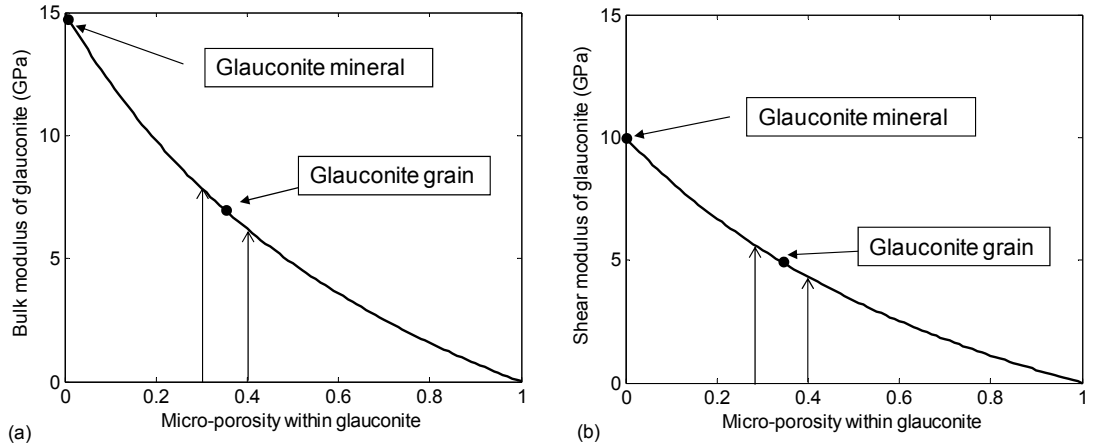

Figure 3.1. *Effective medium modelling of micro-porous glauconite. (a) Bulk modulus and (b) shear modulus of glauconite grain as function of micro-porosity within glauconite by using Hashin-Shtrikman (HS) upper bound. Micro-porosity within glauconite ranges from 30% to 40% for 16 greensand samples and this information was applied to determine the bulk and shear modulus of a micro-porous glauconite grain. Glauconite mineral bulk modulus (15 GPa) and shear (10 GPa) was obtained from Diaz et al. (2002).*

The dominating minerals in greensand are quartz and glauconite. Quartz grains are stiff. Even though glauconite grains are micro-porous, elastic moduli of glauconite mineral are only are reported by Diaz *et al.* (2002). They measured bulk modulus of 15 GPa as bulk and shear modulus of 10 GPa of glauconite mineral from the Cap Mountain Formation, Texas. Because glauconite grains are micro-porous which is physically different from the solid glauconite mineral modulus, it is necessary to calculate the glauconite grain modulus. Hashin-Shtrikman (HS) upper bound (Hashin and Shtrikman, 1963) for mixtures of glauconite mineral and the micro-porosity within glauconite grains was applied for this purpose. Micro-porosity was quantified as the difference between Helium porosity and image macro-porosity as determined from image analysis method (Paper I). Porosity within glauconite was calculated as micro-porosity divided by the amount of glauconite grains as determined by point counting of thin sections (Solymar, 2002; Paper I). Micro-porosity within glauconite varies from 30% to 40% for the 16 greensand samples. By applying these micro-porosities to the HS upper bound, the glauconite grain bulk modulus to be about 7 GPa and shear modulus to be about 5 GPa were determined (Figure 3.1).

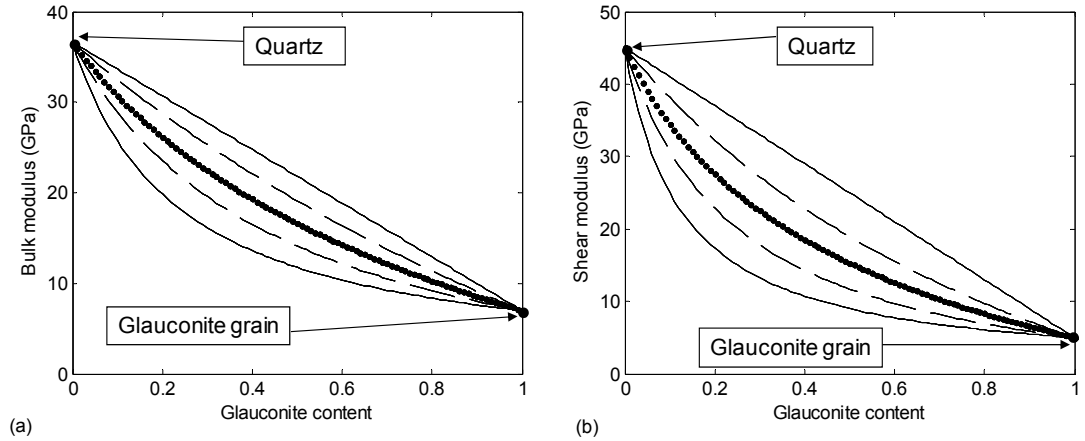

Figure 3.2. *Plots of solid grain elastic moduli of quartz-glauconite mixtures (a) bulk modulus and (b) shear modulus as a function of glauconite fraction. In each figure, the outer two curves represent the Voigt and Reuss Bounds (citation in Mavko et al. 2009). The dashed curves are Hashin-Shtrikman bounds (Hashin and Shtrikman, 1963). The dotted curves in the middle are calculated from Hill's average (Hill, 1952).*

Consider greensand whose grains are mainly quartz and micro-porous glauconite. Bulk and shear moduli of this quartz and glauconite mixture according to Hashin-Shtrikman and Voigt-Reuss elastic bounds are plotted in Figure 3.2. The separation between upper and lower bound depends on how elastically different

the constituents are. The elastic bounds are far apart from each other and from Hill's average (Hill 1952) because of the large elastic contrast between quartz and glauconite grains (Figure 3.2). This implies that the effect of micro-porous glauconite may be critical for seismic greensand interpretation.

3.3 Contact model for mixture of quartz and glauconite grains

The Hertz-Mindlin contact model (Hertz, 1881; Mindlin, 1949; Mindlin et al., 1951) calculates the normal and shear contact stiffnesses of two spherical grains in contact. In this model, grain contacts are first exposed to normal loading, with tangential forces applied afterwards. Walton (1987) described that the effective elastic moduli of the granular assembly are then estimated by taking averages of contact forces corresponding to an assumed distribution of strain over all the contacts. Several authors (e.g., Goddard, 1990; Bachrach et al., 2000; Zimmer, 2003; Makse et al., 2004) have explained the discrepancies between measured data and predictions from the Hertz-Mindlin contact model. Makse et al. (2004) reported that the relation between coordination number and porosity from molecular dynamics simulations usually predicts a lower coordination number than Murphy's empirical relation (Murphy, 1982). To mitigate this overprediction, the modeled effective modulus at the critical porosity is often divided by an ad hoc correction factor, and another ad hoc constant is applied in order to use the frictionless versions of the contact models combined with unrealistically high coordination numbers (Dutta, 2009). DeGennes (1996) suggested that the Hertz model is not valid for granular media. However, Coste and Gilles (1990) have experimentally confirmed the validity of the Hertz single contact model.

Still, the Hertz-Mindlin model appears to be the most commonly used contact model for sandstone. Although the Hertz-Mindlin theory is only applicable to perfect elastic contacts of spherical bodies, it works quite well for sands (Avseth et al., 2005). This model is used to calculate the initial sand-pack modulus of the soft-sand, stiff-sand and intermediate-stiff-sand models. For the initial sand-pack for sandstone, it is assumed that only quartz grains are packed together, and the normal and shear stiffness are calculated based on the contact of two quartz grains. For rocks with mixed mineralogy, a homogeneous mineral modulus is assumed, normally derived using Hill's average (Hill, 1952). Then the normal and shear stiffnesses are calculated based on the contact of two average-

mineralogy grains. However, this is probably only adequate when the moduli of mixed minerals are quite similar. When the mixed minerals are quite different (such as quartz and glauconite) some of the predictive value may be lost (Avseth et al., 2005)

3.4 Hertz-Mindlin modelling for quartz and glauconite

The effective elastic properties of a granular pack of spheres, for which each pair of grains in contact under normal and tangential load determines the fundamental mechanics were investigated in this study. Typically in granular medium models for unconsolidated sand, all grains are taken to be of the same material. So the Hertz-Mindlin contact model for a single type of grain can be found in Mavko et al. (2009). In this study is considered the contact deformation of two grains made of two different minerals, quartz and glauconite, each with the same radius to calculate the effective bulk and shear modulus for a dry pack.

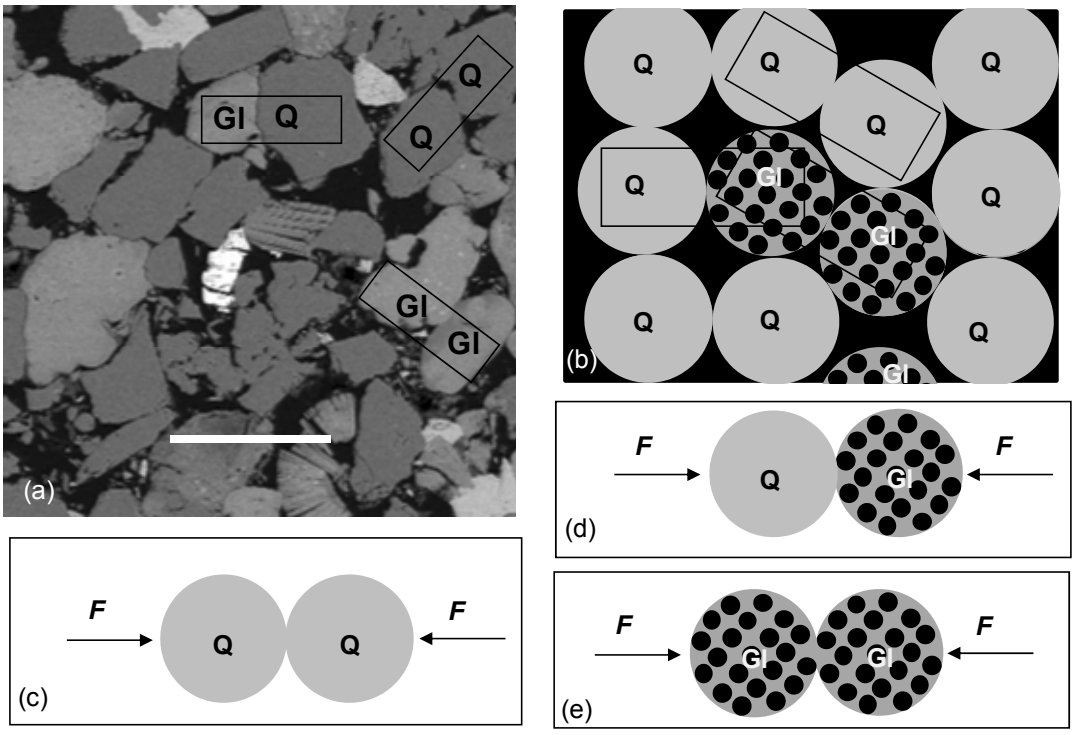

Figure 3.3. *(a) BSE (Backscattered Electron Micrograph) image of the North Sea greensand represents macro-porosity between grains of quartz (Q) and glauconite (Gl). Scale bar for the image is 200 µm. (b) Greensand idealized model. Micro-pores reside within glauconite grains. (c) Schematic representation of Hertz-Mindlin contact model considering quartz and glauconite grains as load bearing (c) quartz-quartz contacts, (d) quartz and glauconite contacts, (e) glauconite-glauconites contacts.*

The derived equations of the Hertz-Mindlin contact model for two types of grains can be found in Paper II. As the amount of quartz grains higher than that of glauconite grains, effective moduli were calculated by balancing among quart-quartz contacts (QQ), quartz-glauconite contacts (QG) and glauconite-glauconite contacts (GG) (Figure 3.1). The elastic moduli a pack of spherical grains are determined from the grains contact area. The grains contact area result from the deformability of grains under pressure.

The P- and S-wave velocities calculated by using the Hertz-Mindlin contact model for two types of grains are presented in Figure 3.4. It is noticed that, in the limit, the Hertz-Mindlin contact model for a single grain type as reported in Mavko et al. (2009) has the same solution as our Hertz-Mindlin model for two types of grains when the fraction of one constituent is 1 and the other is 0 and vice-versa. Calculated velocity for mixtures of quartz and glauconite are higher than velocity calculated from the Hertz-Mindlin contact model for a single grain type by using the effective minerals moduli predicted from Hill's average (Hill, 1952). This demonstrates that the Hertz-Mindlin model with two types of grains may not be approximated by the Hertz-Mindlin single mineral model for a mixture of quartz and glauconite.

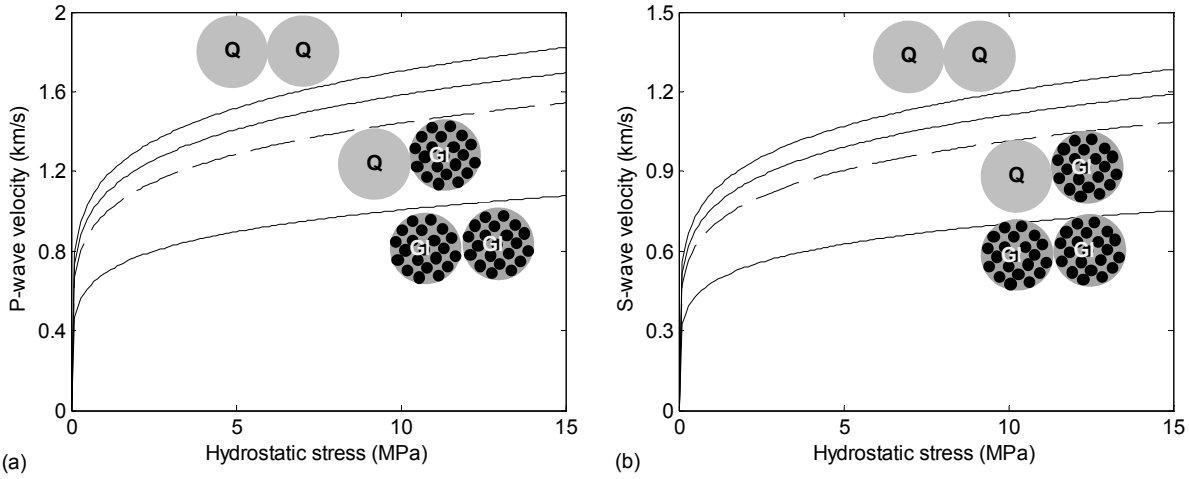

Figure 3.4. *(a) P-wave and (b) S-wave velocity calculated using Hertz-Mindlin contact model with two types of grains. Upper curves are calculated for a quartz fraction of 1 and glauconite fraction of 0. Lower curves are calculated for a quartz fraction of 0 and glauconite fraction of 1. The middle solid curve is calculated for fraction of quartz 0.7 and glauconite is 0.3. The middle dashed curves are from the Hertz-Mindlin contact model for a single grain type by using the effective minerals moduli predicted from Hill's average (Hill, 1952).*

Next, the Hertz-Mindlin model for two types of grains was verified by laboratory experimental results. Figure 3.5 represents the experimental results and results from the Hertz-Mindlin model for two types of grains. From the porosity-coordination number relationship given by Murphy (1982) coordination number 8 was used for this calculation. Thin section analysis shows that this greensand sample is only weakly cemented (Figure 3.3b). For weakly cemented greensand, the Hertz-Mindlin contact model for two types of grains has good agreement with laboratory measured data.

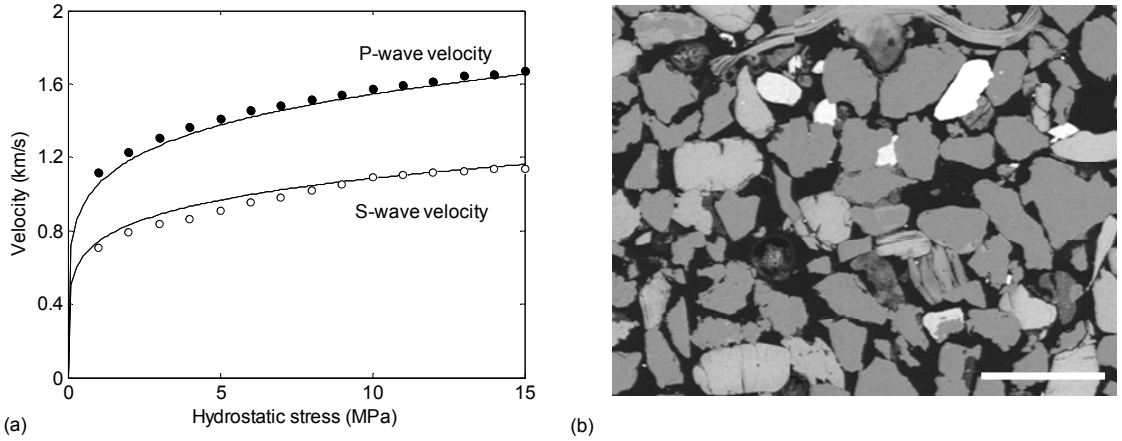

Figure 3.5. *(a) Laboratory measured P-wave velocity (filled circles) and S-wave velocity (open circles) of a weakly cemented greensand and predicted velocity (solid lines) by using Hertz-Mindlin contact model of two types of grains for 70% quartz and 30% glauconite. (b) BSE image of weakly cemented greensand sample.*

3.4 Modelling of the North Sea greensand

Commonly used granular-media models for sandstone are the soft-sand and the stiff-sand models (Dvorkin and Nur, 1996; Mavko et al., 2009). The soft-sand model was introduced by Dvorkin and Nur (1996) for high-porosity sands. The soft-sand model assumes that porosity reduces from the initial sand-pack value due to the deposition of solid matter away from the grain contacts (Figure 3.6). The soft-sand model line is represented by the modified lower Hashin-Shtrikman bound (Hashin and Shtrikman, 1963; Dvorkin and Nur, 1996), and connects the sand-pack porosity end-point and the pure mineral end-point. In the soft-sand model, the effective moduli of the initial sand-pack are computed by the Hertz-Mindlin contact theory (Hertz, 1881; Mindlin, 1949; Mindlin et al., 1951; Mavko et al., 2009), whereas the elastic moduli at the zero-porosity end member are defined by the elastic moduli of the minerals. The porosity reduction between

these points will be a gradual stiffening of the rock, as smaller grains fill the pore-space between the larger grains.

A counterpart to the soft-sand model is the stiff-sand model. The stiff-sand model assumes that porosity reduces from the initial sand-pack value due to the deposition of cement at the grain contacts (Figure 3.6). The stiff-sand model line is represented by the modified upper Hashin-Shtrikman bound (Hashin and Shtrikman, 1963; Mavko et al., 2009), and connects the initial sand-pack porosity end-point and the pure mineral end-point. Like in the soft-sand model, the initial sand-pack modulus of the stiff-sand model is determined by the Hertz-Mindlin theory (Hertz, 1881; Mindlin, 1949; Mindlin et al., 1951; Mavko et al., 2009), whereas the mineral end-point is defined by the elastic moduli of the minerals. The porosity reduction from the initial sand-pack will stiffen the rock, as the contacts between the grains grow.

The intermediate-stiff-sand model fills the interval between the stiff-sand and soft-sand model (Mavko et al., 2009). This model uses the function from the soft-sand model, but the high porosity end-point is situated on the stiff-sand model curve (Figure 3.6). The easiest way to generate these curves is by simply increasing the coordination number of the Hertz-Mindlin theory in the soft-sand model (Mavko et al., 2009). The stiff-sand model explains the theoretically stiffest way to add cement with initial sand-pack, while the soft-sand model explains the theoretically softest way to add pore-filling minerals. However, rocks with very little initial contact cement are not well described by either the stiff-sand or the soft-sand model. In this case, the intermediate-stiff-sand model can be used, because it takes into account the initial cementation effect. Equations for soft-sand model, stiff-sand model and intermediate-stiff-sand model are given in Paper II. The Hertz-Mindlin contact model for two types of grains was used to calculate the initial sand-pack modulus for a soft-sand and a stiff-sand model.

Based on laboratory data, log data, and thin section analysis, a schematic rock-physics model of the North Sea greensand was presented. This model is subdivided into several parts (Figure 3.6):

1. Depositional stage: During the deposition of greensand, quartz and glauconite grains are packed together. In clean greensand, where no diagenetic processes have occurred, the elastic properties of greensand can be calculated by using Hertz-Mindlin contact model for two types of grains (Figure 3.4).

2.1. Lack of silica cementation: At first the marginal parts of the reservoir may have received a major flux of silica from the Sele Formation located in the Siri Canyon in the North Sea (Stokkendal et al., 2009). The silica flux did not influence all parts of the greensand reservoir. For this reason, during this stage, some of the greensand remained unchanged compared to the depositional stage. Elastic properties of this kind of greensand can be calculated by using Hertz-Mindlin contact model for two types of grains (Figure 3.5).

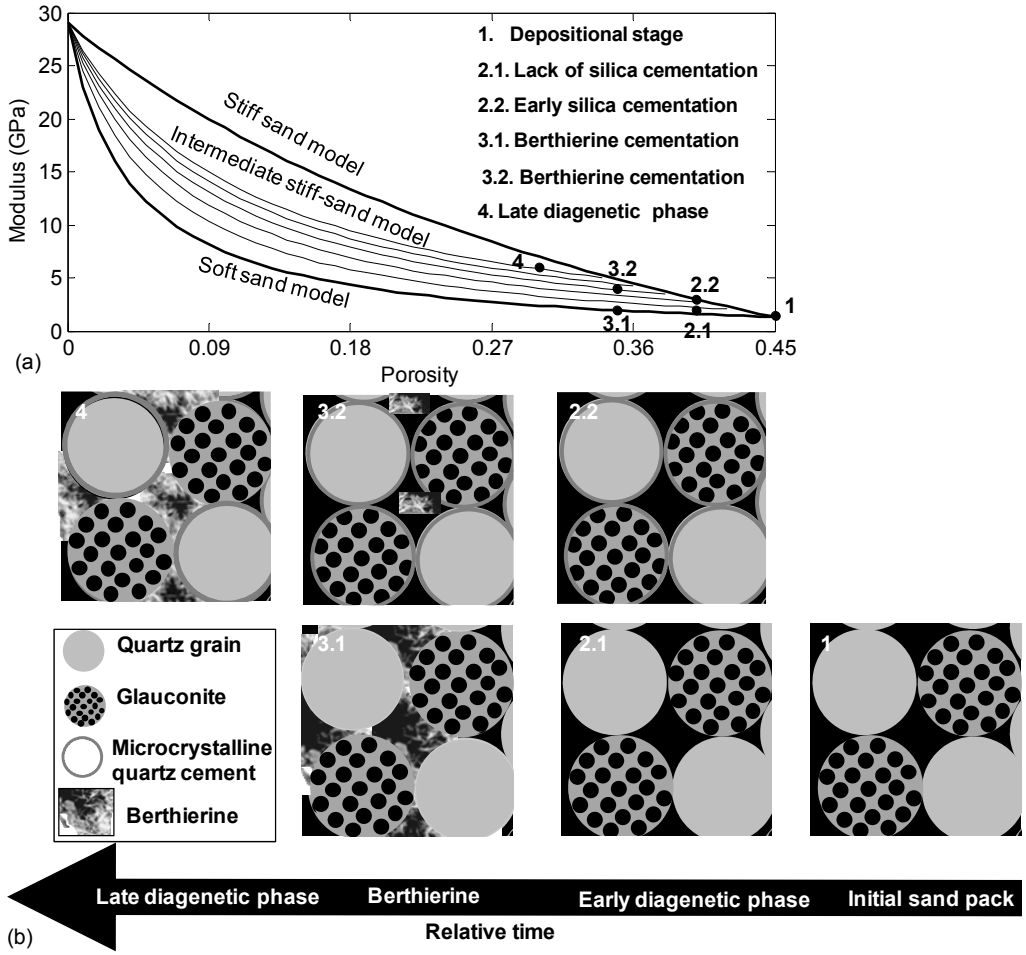

Figure 3.6. *Schematic rock-physics model for the North Sea greensand shows the link between the rock- physics model and greensand diagenesis.*

2.2. Early silica cementation: The first diagenetic mineral to form in the greensand was probably the silica cement. Silica may have formed as an opal rim so that the opal-derived microcrystalline quartz covers all grains. Microcrystalline quartz derived from the opal coating on detrital grains are found in close contact between grains, so this quartz cement has a stiffening effect on

the elastic properties of the greensand. Elastic properties of this kind of greensand may be modeled by an intermediate-stiff-sand or a stiff-sand model.

3.1. Pore-filling berthierine cementation: In the greensand reservoir, where microcrystalline quartz cement is absent, berthierine precipitates between the grains, so porosity of this kind of greensand decreases from the initial sand-pack porosity. This kind of greensand can be modeled by a soft-sand model.

3.2. Berthierine in early silica-cemented greensand: Berthierine also precipitates in greensand, where microcrystalline quartz cement is present. Berthierine precipitation between the grains causes major porosity reduction. Elastic properties of this kind of greensand may be modeled by an intermediate-stiff-sand or a stiff-sand model.

4. Late diagenetic phase: If berthierine continues its growth in the pore space, the elastic properties of this kind of greensand may be modeled by an intermediate-stiff-sand or a stiff-sand model.

4. Vp-Vs relationship and AVO modelling

4.1 Vp-Vs relationship of greensand

An important part of rock physics modelling is the V_p-V_s relationship. The V_p-V_s relationship is normally used to predict V_s where only V_p is known. V_p-V_s relationships are also used for AVO analysis and to identify the pore fluids from seismic data. Without V_s it is often difficult to separate the seismic signature of lithology and pore fluids. Furthermore, V_s may also provide information for distinguishing between pore pressure and saturation changes in 4D seismic data and also provide the means for obtaining images in gassy sediments where P-wave is attenuated (Avseth et al., 2005). Therefore, in most cases when V_s is not available or is difficult to obtain, a V_p-V_s relationship is used to calculate V_p from V_s. The V_p-V_s relationship can also be used as a quality control tool even when V_s information is available. Therefore several authors developed physical as well as statistical empirical V_p-V_s relationships to predict V_s from V_p (e.g. Pickett, 1963; Milholland et al., 1980; Castagna et al., 1985; Krief et al. 1990; Greenberg and Castagna, 1992; Han, 1986a; Han et al., 1986b; Xu and White, 1995, 1996; Vernik et al., 2002; Williams, 1990).

Pickett (1963) provided V_p-V_s relations for limestones and dolomite. The relation by Vernik et al. (2002) is nonlinear and works for sandstones. Greenberg and Castagna (1992) have given empirical relations to predict V_s from V_p by taking into account complex lithologies. Xu and White (1995) demonstrated a theoretical model to determine the V_p-V_s relationship of shaly sandstone by mixing two inclusion models with different aspect ratios of pores, which represent respectively sandstone and shale portions. By using dataset from the North Sea, Jørstad et al. (1999) compared the model developed by Xu and White (1995) and concluded that the inclusion models need to be calibrated well by well, whereas the simple regression tuned to the target wells provide good prediction of V_s from the measured V_p. Tsuneyama (2005) presented theoretical assessments of the validity of several known regressions by using effective medium theory and discussed how one should consider modifying the known relationship depending on the character of the target rock.

Castagna et al. (1985) published the most widely used empirical V_p-V_s relationships for rock types including sandstone, mudrock, limestone and

dolomite. The empirical V_p-V_s relationship for sandstone offered by Castagna et al. (1985):

$$V_S = 0.80V_P - 0.86 \ \textit{(km/s)}, \tag{4.1}$$

and the mudrock line of Castagna et al. (1985), which was derived from *in-situ* data:

$$V_S = 0.86V_P - 1.17 \ \textit{(km/s)}. \tag{4.2}$$

Castagna's regressions provide reasonable results to predict V_s for consolidated rocks with P-wave velocities greater than about 2.6 km/s.

Han et al. (1986a) provided an empirical relationship based on ultrasonic laboratory measurements for clay bearing sandstone:

$$V_S = 0.79V_P - 0.79 \ \textit{(km/s)}. \tag{4.3}$$

The relations from Castagna et al. (1985) and Han et al. (1986a) for sandstone are essentially the same and give a reasonable average when lithology is not well constrained (Mavko et al., 2009).

Figure 4.1 shows a plot of V_s versus V_p of laboratory measured brine saturated greensand samples. From these data an empirical V_p-V_s regression of laboratory measured brine saturated greensand can be approximated by the least-squares linear fit:

$$V_S = 0.76V_P - 0.76 \ \textit{(km/s)}. \tag{4.4}$$

The dataset fall along a narrow trend, in spite of variation in porosity, variation in greensand cementation and a confining pressure ranging from 1 to 12 MPa. Even though porosity tends to decrease velocity; clay also tends to lower velocity and confining pressure tends to increase velocity. From the dataset of Han et al. (1986b), Avseth et al. (2005) showed that for clay bearing sandstone, porosity, clay and confining pressure act approximately similarly on V_p and V_s so that the

data stay tightly clustered within the same V_p-V_s trend. V_p-V_s relations derived from Iso-frame model (details in Paper III) is:

$$V_S = 0.95V_P - 1.127 \ \textit{(km/s)} \qquad (4.5)$$

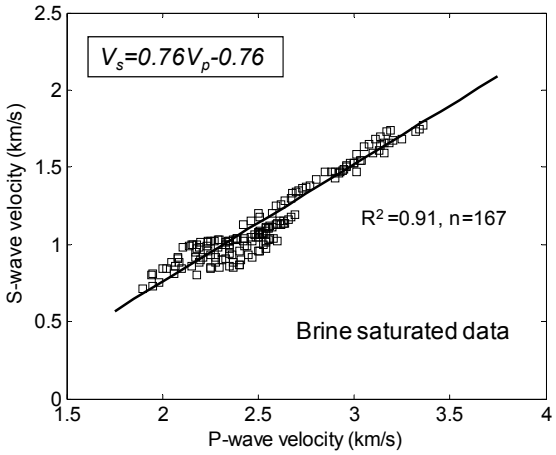

Figure 4.1. *Linear regression between laboratory Vp and Vs data on brine saturated at hydrostatic confining pressure with steps 1 MPa to 12 MPa.*

Predicted V_s and measured V_s agree well by using empirical V_p-V_s regressions of greensand and the V_p-V_s relationship derived from modelling. Figure 4.2 shows the comparison of measured and predicted V_s velocity by using different V_p-V_s regressions. Predictions using the Iso-frame model are quite well although high V_s tend to be overpredicted and low V_s tend to be under predicted (Figure 4.2a). Comparisons between measured and predicted shear wave velocity were quantified by statistical analysis in terms of rms (root mean square) error and r^2 (coefficient of determination). The rms error is 8% and r^2 is 0.9 in the empirical V_p-V_s regression obtained from laboratory data. However, the rms errors are comparatively higher (10%) and the r^2 are comparatively lower (0.82) when using the relation derived from the Iso-frame model.

Although published V_p-V_s relationships for clay bearing sandstone by Han *et al.* (1986a) and for sandstone by Castagna *et al.* (1985) give a reasonable average to predict shear wave velocity when other alternative relationships are unavailable, for greensand they are not consistent. The regression reported by Han et al. (1986a) for clay bearing sandstone underestimates the velocity (Figure 4.2b) while the mudrock line by Castagna et al. (1985) over-estimates the velocity (Figure 4.2c). However, predictions are quite good when using the regression

reported by Castagna et al. (1985) for sandstone (Figure 4.2d) and the rms error is 8% and r^2 is 0.88 for this regression. While the rms error is 11% and r^2 is 0.81 by using the regression for clay bearing sandstone reported by Han *et al.* (1986). The rms error is the highest (16%) and r^2 is the lowest (0.63) for the mudrock line (Castagna et al., 1985). Obviously the mudrock line was derived for shales and should not be used for greensands. Nevertheless, the statistical analysis shows that rms error and r^2 for greensand, for clay bearing sandstone by Han et al. (1986a) and for sandstone by Castagna et al. (1985) are close to each other. Therefore, any of these three may be used to predict the shear wave velocity for greensand.

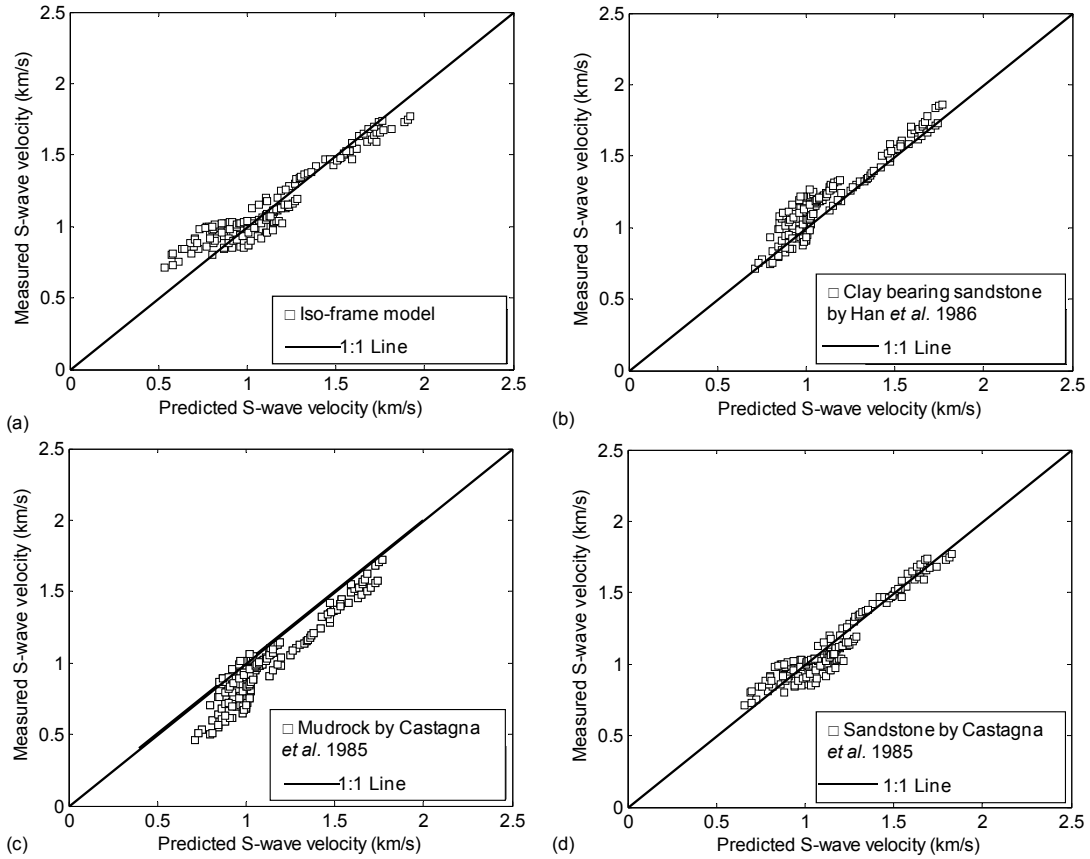

Figure 4.2. *Comparison between predicted and measured shear wave velocities: (a) by using V_p-V_s relationship obtained from the effective medium Iso-frame model, (b) by using regression by Han et al. (1986) for clay bearing sandstone, (c) by using Mudrock line by Castagna et al. (1985), and (d) by using regression by Castagna et al. (1985) for sandstone.*

4.2 AVO modelling of greensand

AVO modelling is a step in multidisciplinary integration of petrophysics, rock physics, seismic data and geology as well as petroleum engineering. AVO

modelling is also used to examine the potential use of AVO. To predict the lithology and pore fluid from seismic data are the main objective for AVO analysis (Castagna and Smith, 1994; Castagna et al. 1993; Castagna et al. 1998; Lie et al., 2007). However, Avseth et al. (2005) pointed out that in many cases AVO has been applied without success and that lack of information on shear wave velocity and the use of a too simple geological model are some of the common reasons for failure. Moreover, lithology has significant impact on AVO response which may induce AVO anomalies (Avseth, 2000). Therefore, the understanding of the AVO response based on local geology is important before using it for reservoir characterization.

AVO curves were calculated for glauconitic greensand and quartzitic sandstone each capped by shale. Figure 4.3 represents the PP reflection coefficient (R_{PP}) as a function of incident angle ranging from 0^o to 30^o. Zoeppritz's equations as given in Mavko et al. (2009) were used to calculate the reflection coefficient. Data for sandstone with brine and oil were obtained from Castagna and Swan (1997). Shale data for AVO curves were obtained from the studied Nini 1A well. The shale represents the cap-rock for both greensand and quartzitic sandstone. For greensand, the mean values of V_p, V_s and density of laboratory measured sixteen dry greensand samples were used as input to calculate the reflection coefficient. Data representing the brine and oil saturated state were calculated by using Gassmann's equation (Gassmann 1951). The calculated reflection coefficient is displayed as the thin line on the plot as calculated from mean values of V_p, V_s and density, whereas the gray band represents the range of reflection coefficients as calculated from the maximum and minimum values of V_p, V_s and density. The corresponding AVO response shows a negative zero-offset reflectivity and a positive AVO gradient. AVO responses of brine saturated quartzitic sandstone and brine saturated greensand are distinguishable both at zero and far offset. Oil saturated sandstone and oil saturated greensand are also distinguishable both at zero and at far offset. Although both greensand and quartzitic sandstone are capped by elastically similar shale, greensand produces a stronger negative reflector. However, it is also noticeable that brine saturated greensand may have similar AVO response to oil saturated quartzitic sandstone. The observed difference in seismic response between the greensand and the quartzitic sandstone is due to the difference in grain composition. Thus if the difference between greensand and quartzitic sandstone is ignored, their difference in AVO response could be interpreted as being due to pore fluid.

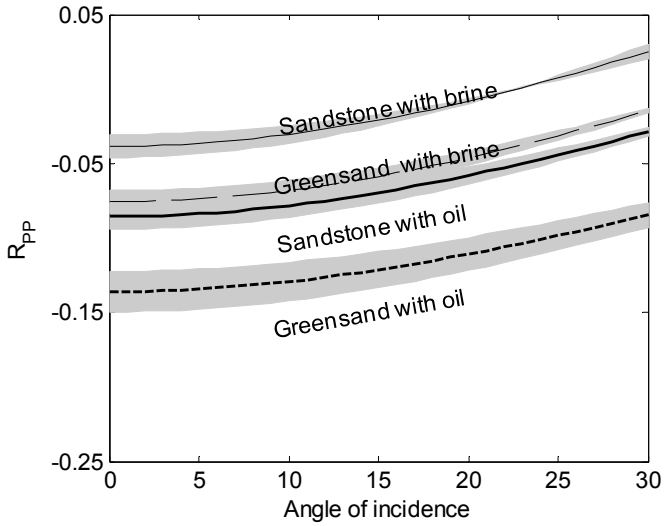

Figure 4.3. *AVO curves for greensand and sandstone capped by shale, in the brine and in the oil saturation condition. PP reflection coefficients were calculated by using Zoeppritz's equations. The brine saturated greensand and oil saturated sandstone have almost similar AVO response. Errors in calculation of reflection coefficient are presented by shaded bands.*

Next, AVO modelling of two types of greensand (the weakly cemented and the cemented) defined by petrographic image analysis and core analysis presents in Figure 4.4. Figure 4.4 represents the PP reflection coefficient as a function of incident angle ranging from 0^o to 30^o calculated from Zoeppritz's equations as given in Mavko et al. (2009). The mean values of V_p, V_s and density of the laboratory measured four greensand samples from Hermod Formation are used as input to calculate the reflection coefficient of weakly cemented greensand, whereas the mean values of V_p, V_s and density of the laboratory measured four samples from Ty Formation are used as input to calculate the reflection coefficient of cemented greensand. Data for the brine and the oil saturated state were calculated using Gassmann's equation (Gassmann, 1951). The calculated reflection coefficient is displayed as the thin line on the plot as calculated from mean values of V_p, V_s and density, whereas the gray band represents the range of of reflection coefficients as calculated from the maximum and minimum values of V_p, V_s and density.

AVO responses of brine saturated weakly cemented greensand and brine saturated cemented greensand are distinguishable both at zero and far offset. Oil saturated weakly cemented greensand and oil saturated cemented greensand are also distinguishable both at zero and far offset. Hydrocarbons cause a stronger negative reflection coefficient, whereas cementation causes a more positive

reflection coefficient. It is also noticeable that oil saturated cemented greensand may have similar AVO response to brine saturated weakly cemented greensand. The observed difference in the seismic response between the two types of greensand is due to the difference in greensand diagenesis. Small amounts of berthierine and microcrystalline quartz cement in Ty Formation greensands cause a difference in seismic response. Thus if difference between cemented greensand and weakly cemented greensand is ignored, their difference in AVO response could be interpreted as being due to pore fluid.

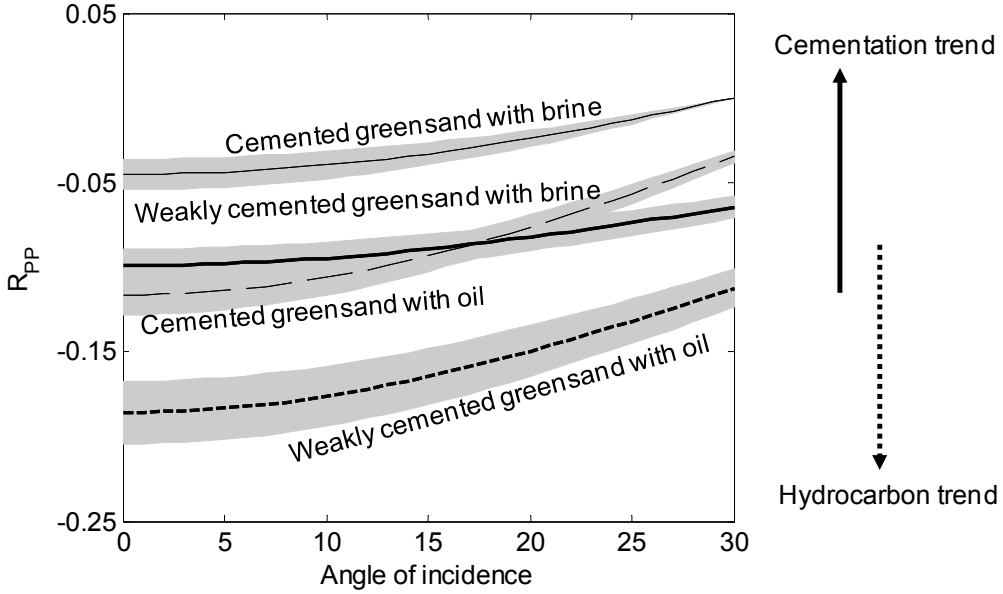

Figure 4.3. *AVO curves for weakly cemented greensand and cemented greensand capped by shale, in the brine and in the oil saturation condition. PP reflection coefficients were calculated by using Zoeppritz's equations. The brine saturated weakly cemented greensand has about the same AVO response as oil saturated cemented greensand. Errors in calculation of reflection coefficient are presented by shaded bands.*

Shale as a cap-rock was used during AVO modelling. Shale can be anisotropic and anisotropy of the cap rock would influence the AVO analysis. Blangy (1992) showed how transverse isotropy of shaly cap-rocks could drastically influence the AVO response of a reservoir. However, Avseth et al. (2008) studied the effect of shale intrinsic anisotropy on AVO signatures of sandstones reservoirs capped by shale and found that the anisotropy effect became significant beyond about 30^0 angles of incidence. Therefore, the effect of anisotropy on AVO was disregarded in this study.

5. Fluid substitution in greensand

Fluid substitution is the heart of rock physics. Fluid substitution is used to predict how the seismic velocity depends on pore fluids. Gassmann's equations (Gassmann, 1951) are simple, robust and widely used to predict rock moduli changes with a change of pore fluids. However, several studies show that the predictions from Gassmann's equations not always match observations (Fabricius et al., 2010; Adam et al., 2006; Coyer, 1984; Assefa et al., 2003; Røgen et al., 2005; Batzle et al., 2006; Baechle et al., 2009). Gassmann's equations generally work at low frequency and do not take into consideration the fluid related dispersion (Berryman, 1980). Biot's flow or global flow (Biot, 1956a, Biot, 1956a) is often used to describe the fluid related dispersion. At low frequency the fluids move with solid part of rock. While at high frequency the pore fluid lag behind the solid part and generate the Biot's flow. Biot's characteristic frequency (f_c) is used to describe the transition between high frequency and low frequency for the Biot's flow as cited by Mavko et al. (2009):

$$f_c = \frac{\phi\eta}{2\pi\rho_f k}, \tag{5.1}$$

where, η is fluid viscosity and ρ_f is fluid density, ϕ is porosity and k is permeability. Biot's low frequency limiting velocities are the same as those Gassmann relations (Mavko et al., 2009).

However, several studies also showed that Biot's theory does not fully explain the frequency dispersion for natural saturated rocks and the calculated frequency dispersion is usually less than three percents for most reservoir rocks (Winkler, 1983; Winkler, 1985; Winkler, 1986; Wang and Nur, 1988 and Mavko and Jizba, 1991). Winkler (1983) studied the Berea sandstone and found a dispersion of two percent from low to high frequency by using Biot's theory. Fluid flow from compliant pores to less compliant pores can cause local flow or squirt flow (Mavko and Nur, 1979; Murphy, 1982; Murphy, 1984; Winkler, 1983; Winkler, 1985; Winkler, 1986). By squirt relations, Mavko and Jizba (1991) show that water saturated rock may have larger velocity dispersion than would be predicted from Gassmann's equations and even predicted from Biot's high frequency case. Mavko et al. (2009) suggested that in most crustal rocks the amount of squirt dispersion is comparable to or greater than Biot's dispersion, and thus using

Biot's theory alone will lead to poor predictions of high-frequency saturated velocities. Spencer (1981) described that total dispersion may be described by Biot's dispersion together with squirt dispersion.

5.1 Gassmann's method

Gassmann predicted saturated bulk modulus from dry bulk modulus should be equal to measured saturated bulk modulus if fluid related dispersion is insignificant. In the same way dry shear moduli should be equal to saturated shear moduli. However, there are some differences between them (Figure 5.1). Input parameters used in the Gassmann model are the dry bulk modulus, *K dry* computed from the dry P- and S-wave velocity data, the porosity, fluid bulk modulus and mineral bulk modulus (K_o). Fluid bulk modulus fluid is 2.9 GPa as calculated from Batzle and Wang (1992) relations as cited by Mavko et al. (2009). K_o is 33 GPa calculated as the effective mineral bulk modulus of greensand (Hossain et al., 2010d). Variation of the mineral bulk modulus within a reasonable range of ±5 percent has a negligible impact on the computed P- and S-wave velocities for sandstones (Mavko and Jizba, 1991). The sensitive analysis by Sengupta and Mavko (2003) also showed that Gassmann fluid substation method is only little sensitive to the mineral modulus of rock.

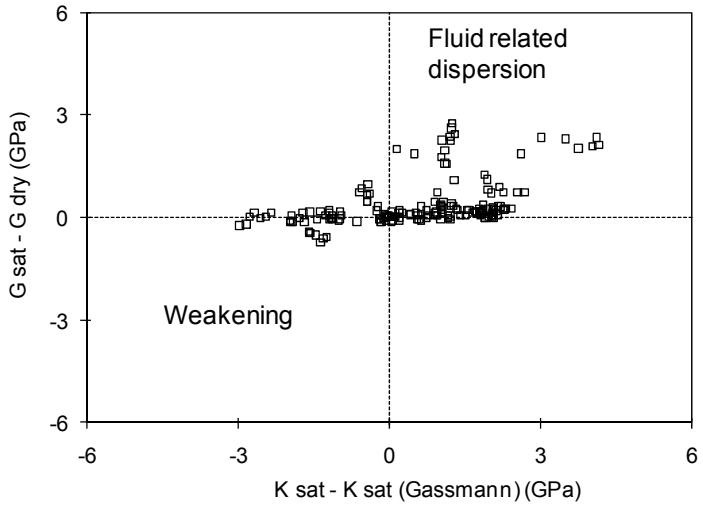

Figure 5.1. *Difference between measured and Gassmann's predicted bulk and shear moduli.*

Measured saturated moduli lower than Gassmann's predicted saturated moduli may be due to the water weakening effect of greensand. One of the assumptions of fluid substitution models is that the pore fluids do not interact with the matrix

in such way that would soften the frame. In fact pore fluid may interact with solid matrix to changes the surface energy. Water weakening of saturated rocks is described by several authors (e.g. Wang, 2001; Røgen et al., 2005; Fabricius et al., 2010; Røgen et al., 2005). Gassmann's theory does not take into consideration the fluid related dispersion. Therefore measured saturated moduli higher than Gassmann's predicted saturated bulk moduli may be due to fluid related dispersion. Fluid related dispersions are expected if during the acoustic measurement due to high frequency the fluid would contribute to stiffen the rocks.

5.2 Biot's method

In order to check whether moduli dispersion will occur due to the high frequency Biot's flow, the characteristic frequency (f_c) for the Biot's flow was calculated. As Biot's flow occurs for wave frequency in the kHz to the MHz range, Biot's flow will occur in the North Sea greensand (Figure 5.2a). In Figure 5.2b however it is shown that Biot's flow will occur only in the large pores. Biot's flow should not occur in micro-pores. Fabricius et al. (2010) showed the relationship between Biot's reference frequency and specific surface of pores. In the same way a relationship between NMR T_{2i} and f_c may be obtained from Kozeny's equation (combining equation 2.7 and 5.1):

$$f_c = \frac{\eta}{2\pi\rho_f c(T_{2i}\rho_2)^2}. \qquad (5.2)$$

From equation (5.2) it is clear that each particular pore size has a characterized frequency and that can vary from GHz to kHz (Figure 5.3a). Even though cutoff time for micro-porosity is 5.1 ms, cutoff time for Biot's flow may be defined as 68 ms. Then it is clear that Biot's flow should occur only in the larger pores, whereas intermediate and micro-pores will not contribute to Biot's flow (Figure 5.3c). So Biot's flow should not occur in around in 18% porosity out of 38% porosity of this sample (Figure 5.3d).

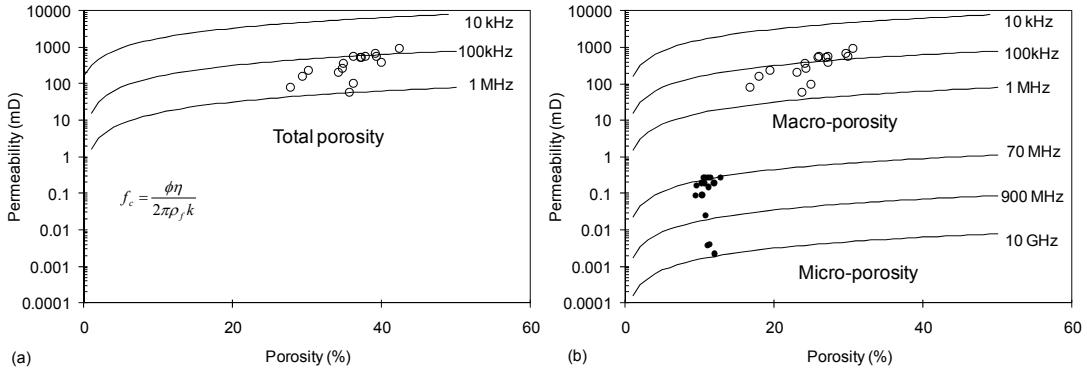

Figure 5.2. *(a) Cross plot of total porosity versus total permeability of greensand samples. Reference curves represent the permeability of Biot's flow as calculated by using Biot's critical frequency equation (5.1). As Biot's flow occurs for wave frequency in the kHz to the MHz range, Biot's flow will occur in the North Sea greensand. (b) Cross plot of macro-porosity versus permeability in large pores (open circles) and micro-porosity versus permeability in micro-pores (closed circles). Reference curves represent the permeability of Biot's flow as calculated by using Biot's critical frequency equation (5.1). Biot's flow will occur only in the macro-pores, while Biot's flow should not occur in the micro-pores.*

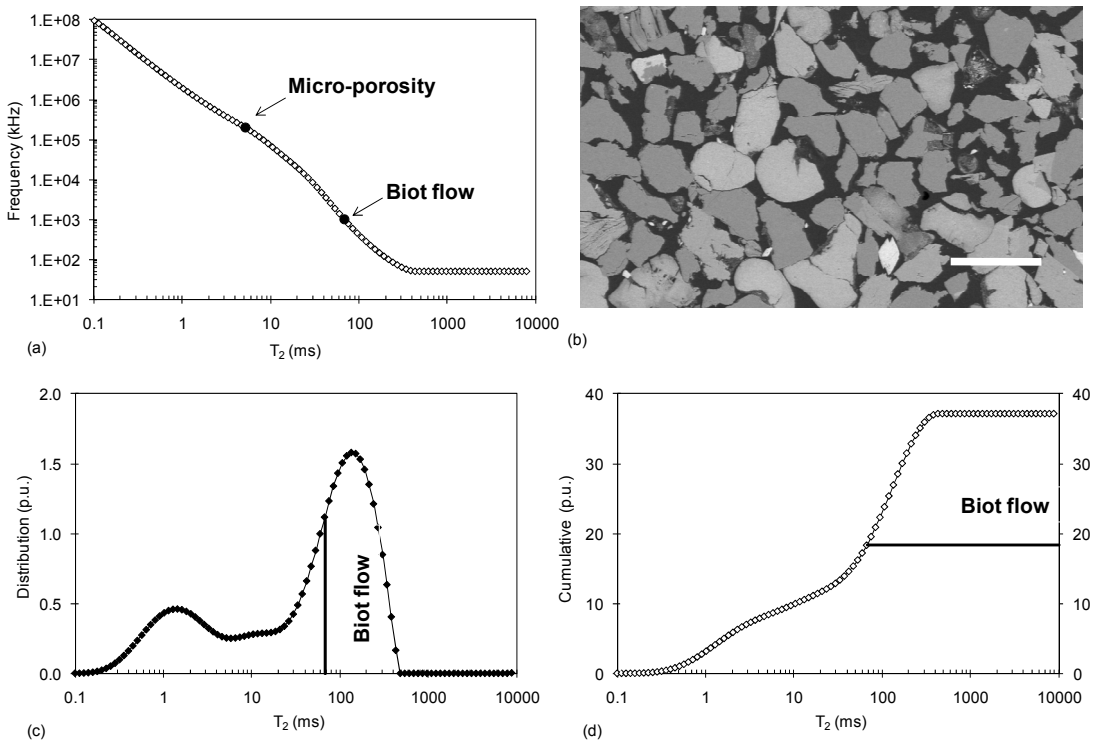

Figure 5.3. *(a) NMR T_2 distribution versus frequency as calculated by using Biot's critical frequency equation (5.2), (b) BSE image of this sample. (c) Porosity distribution from NMR measurement together with cutoff time of Biot's flow, (d) cumulative porosity from NMR measurement together with cutoff time of Biot's flow.*

5.3 Squirt method

In squirt flow mechanisms, the local flow in small cracks gives rise to a local stiffening pressure gradient in the fluid. A schematic diagram of squirt flow could be very similar to the greensand model if local flow in macro-porosity gives rise to local stiffening pressure gradient in the fluid (Figure 5.4).

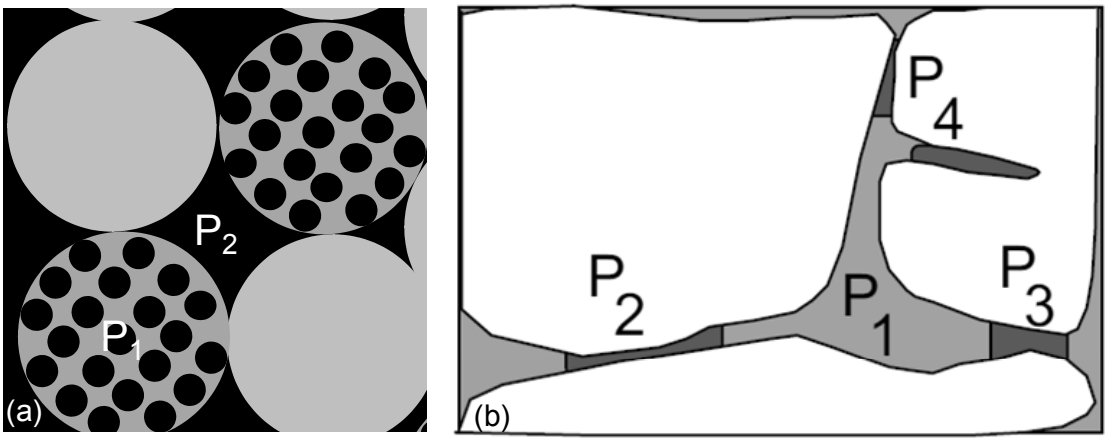

Figure 5.4. *(a) Greensand model, (b) schematic diagram of squirt flow (Mavko and Jizba, 1991).*

In order to check whether differences of fluid flow in macro-pores and micro-pores pores are related with local flow or squirt flow, the squirt model was used to predict high frequency unrelaxed saturated bulk modulus for sample 1-18 from dry bulk modulus. Figure 5.5 shows that comparison among the observed laboratory data, high-frequency predictions of Biot's (1956a, b), and low frequency predictions of Gassmann's (1951). Input parameters used in the Biot's model are the dry bulk modulus, *K dry* computed from the dry P- and S-wave velocity data, the porosity, fluid bulk modulus and mineral bulk modulus. In addition, a tortuosity factor set equal to 2 is used in the Biot's model. Variation of tortuosity within a typical range of one to three has a negligible impact on calculated moduli (Mavko and Jizba, 1991). Both Gassmann and Biot's methods under predicted the saturated bulk modulus (Figure 5.5). To calculate high-frequency saturated unrelaxed bulk moduli the unrelaxed frame bulk moduli were calculated, then these unrelaxed frame bulk moduli were used in Biot's model to estimate the high-frequency saturated unrelaxed bulk moduli. The high frequency unrelaxed bulk moduli agree with laboratory measured data when unrelaxed frame moduli are calculated by using micro-porosity of 20% as the soft porosity in a squirt model. It is clear that total fluid related dispersion in greensand may be explained by combining Biot's flow and squirt flow (Figure 5.5). Biot's

dispersion is much lower than squirt dispersion. Biot model may not be enough to describe the fluid related dispersion of this greensand sample.

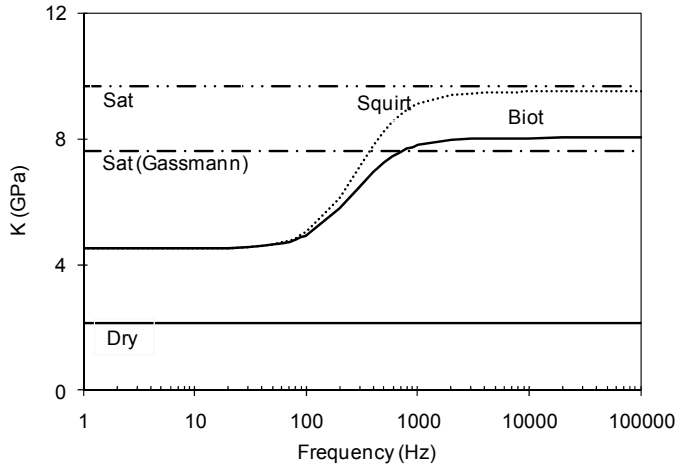

Figure 5.5. *Comparison of laboratory measured brine saturated bulk moduli with predicted saturated moduli from dry bulk moduli. Both Gassmann and Biot's methods are under predicted the saturated bulk modulus. Predictions by using squirt model are comparable with laboratory measured data when soft porosity is assumed around 20%.*

6. CO_2 injection effect on physical properties of greensand

At reservoir condition, CO_2 may affect the aquifer properties in two ways. Firstly, CO_2 dissolved in water is in equilibrium with carbonic acid. The acid may react with the rock thus changing its physical and mechanical properties. Secondly, when CO_2 is injected into a reservoir formation, the existing formation fluid in pore space will be partially displaced by CO_2 thus changing the compressibility and density of the reservoir rock.

Time-lapse seismic surveys currently provide the most attractive approach to monitoring compressibility and density of reservoir rocks. However, understanding the changes of seismic signature due to CO_2 injection is the key element in monitoring the injection of CO_2. Several studies show that based on rock physics modelling, it is possible to discuss how reservoir properties are affected seismically during CO_2 flooding (Wang et al., 1998; Xue and Ohsumi, 2004; Siggins, 2006; Brown et al., 2007; Lei and Xueb, 2009). Gassmann's equations (Gassmann 1951) are generally used to calculate the seismic response due to changing pore fluid. Gassmann's equations (Gassmann 1951) are also used to calculate the seismic response of CO_2 bearing rocks (McKenna et al., 2003; Lei and Xueb, 2009 and Wang et al., 1989; Wang, 2000; Kazemeini et al., 2010; Carcione et al., 2006). Compressibility and density of fluids are necessary input parameters for these calculations. When CO_2 is injected into water-saturated rock and CO_2 dissolves in the brine, it will change the physical properties of brine. Therefore, a correction of fluid properties is required based on compressibility and density as function of dissolve CO_2 in the brine. AVO is also used to calculate the CO_2 bearing rock's seismic response (Brown et al., 2007 and Morozov, 2010). AVO is a method that combines V_p, V_s and density, it will be more sensitive to changes in CO_2 saturation than a method that relies on V_p only. Therefore, since AVO depends on both the velocities and density, the AVO response should be sensitive to an extended range of CO_2 saturations.

6.1 Effect of CO_2 injection on petrophysical properties

In general, helium porosity, specific surface area by BET method, grain density and electrical resistivity before and after the CO_2 injection remain unchanged considering the error of measurements (Figure 5 in Paper IV).

The NMR T_2 distributions are presented in graphical form for one greensand sample before and after the CO_2 flooding experiment (Figure 6.1a). Sample 1A-142 shows that that the smaller peaks become slightly smaller whereas the larger peaks are shifted to larger time after CO_2 injection. Cutoff values 5.2 ms for the sample from Hermod Formation and 3.7 ms for the samples from Ty Formation were used to determine the macro-porosity and micro-porosity from NMR T_2 distribution. Micro-porosity remains largely unchanged from before to after CO_2 injection (Figure 6.1b). Whereas, macro-pore size tends to increase after CO_2 injection (Figure 6.1b).

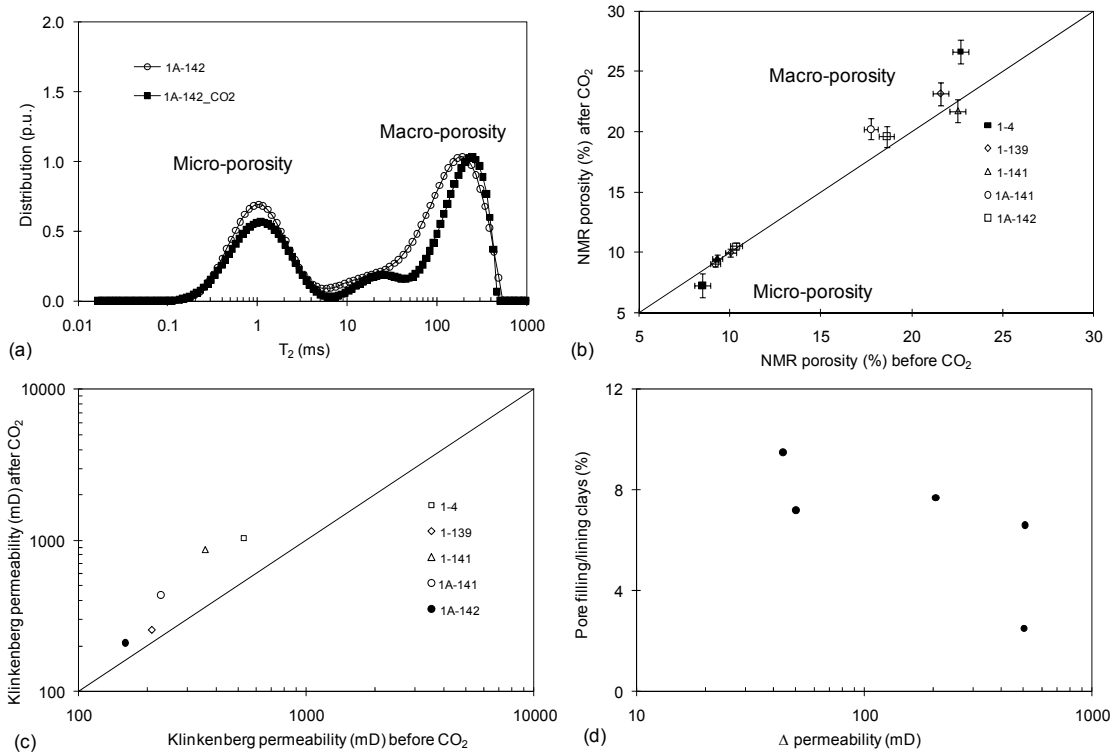

Figure 6.1. *(a) NMR T_2 distribution of a greensand in porosity units (p.u.) before and after CO_2 injection, (b) Macro-porosity and micro-porosity as determined from NMR measurements before and after CO_2 injection. (c) Laboratory measured Klinkenberg permeability before and after the CO_2 injection, (d) cross-plot of delta permeability (permeability after CO_2 injection minus permeability before CO_2 injection) versus amount of pore filling clay minerals.*

Klinkenberg permeability increased by a factor 1.26-2.4 due to the CO_2 flooding experiment (Figure 6.1c). The increased permeability could in principle be explained by sample fracturing and/or migration of fine particles during the CO_2 flooding experiment. Micro-crystalline quartz and pore-filling minerals (Fig. 1b) have significant effect on formation permeability (Stokkandel et al., 2009). During the CO_2 flooding experiment, lose fine particles of pore-filling or pore-

lining clay could be shifted around which could cause the increase in permeability. This possibility is corroborated by the inverse trend between change in permeability and amount of pre-filling/lining clay minerals (Figure 6.1d).

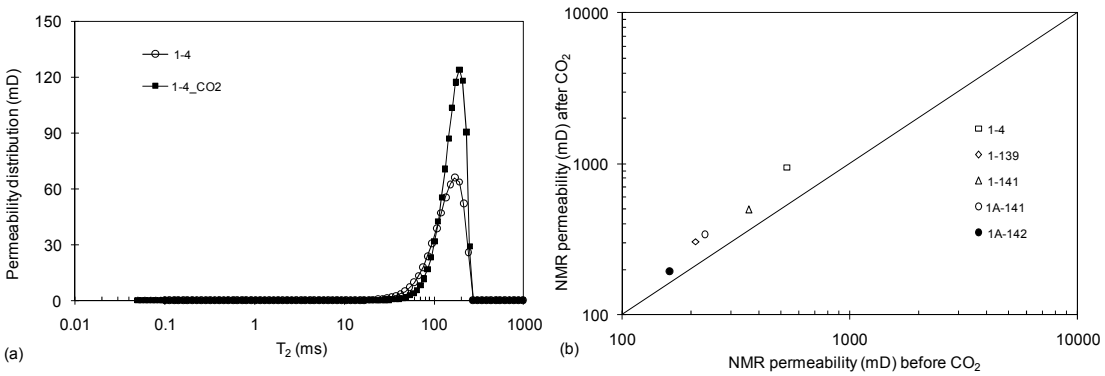

Figure 6.2. *(a) NMR permeability distribution in mD before and after CO_2 injection as calculated from permeability modelling. (b) NMR predicted permeability before and after CO_2 injection.*

In order to evaluate whether the permeability change is due to matrix effects alone, the NMR permeability model provided in section 2 was used to compare NMR predicted permeability before and after CO_2 injection. An example of predicted permeability distribution obtained by using Equation 2.8 is shown in Figure 6.2a. Below 5.2 ms, the amplitude of permeability is close to zero which means micro-porosity does not contribute significantly to fluid flow. From 5.2 ms to 100 ms, the amplitude of permeability is small but above 100 ms the contribution to permeability increases. NMR predicted permeability after CO_2 injection tends to increase (Figure 6.2). From NMR permeability distribution, it is clear that permeability is dominated by the size of macro-pores in the greensand. So NMR predicted permeability after CO_2 injection increases due to the increasing the size of macro-pores. The increase of macro-pores size is probably due to migration of fine pore-filling minerals. The increase in Klinkenberg permeability can thus not be explained by fracturing.

6.2 Effect of CO_2 injection on elastic properties

P-wave and S-wave velocity for the brine saturated condition are almost constant before and after the CO_2 flooding experiment (Figure 6.3a and Figure 6.3b). Even though P-wave and S-wave velocity for dry condition show more scatter

before and after CO_2 injection, they probably remain unchanged (Figure 6.3c and Figure 6.3d).

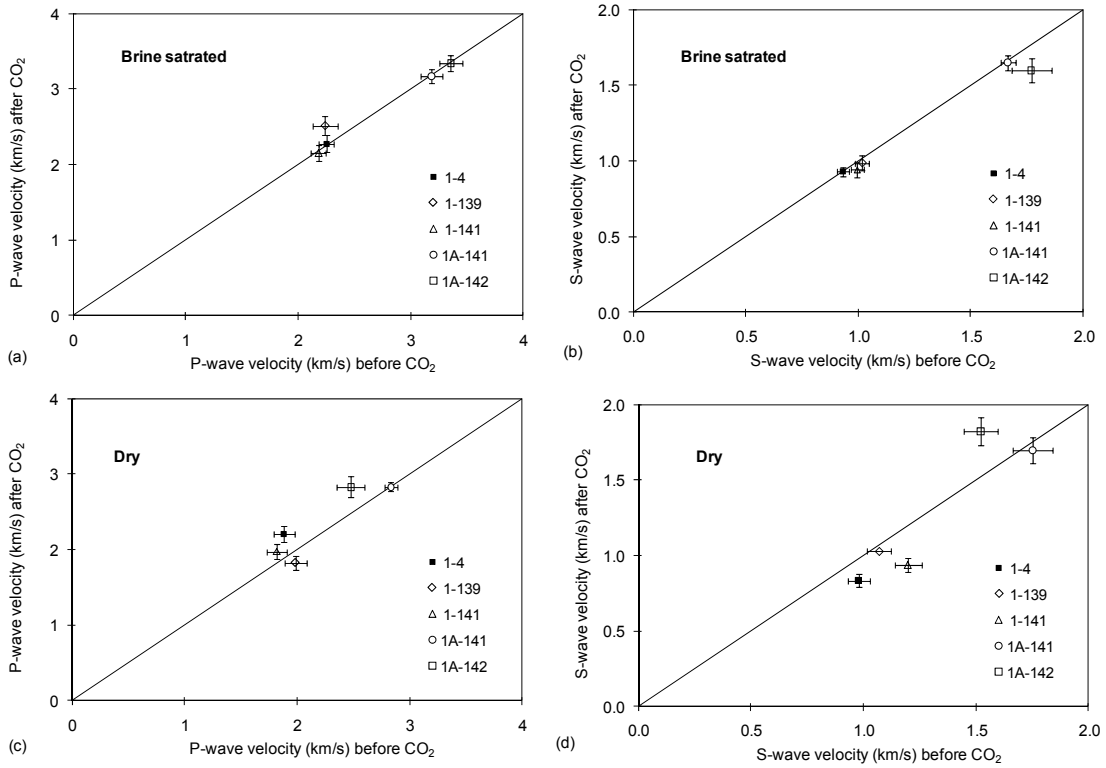

Figure 6.3. *Laboratory measured (a) P-wave velocity and (b) S-wave velocity of brine saturated greensand samples before and after the CO_2 injection. Laboratory measured (c) P-wave velocity and (d) S-wave velocity of dry greensand samples before and after the CO_2 injection.*

6.3 Rock physics and AVO modelling of CO_2 bearing greensand

By using Gassmann's equations calculated P-wave velocity and S-wave velocity of CO_2 bearing greensand samples are presented in Figure 6.4a. The modelling results demonstrate that the largest changes in CO_2 saturated properties occur when the first small amounts of CO_2 are injected into brine saturated greensand. At higher CO_2 saturation levels, the change in elastic properties is relatively small. Modelling results show that the effect of CO_2 flooding decreases V_p by 2%-41% relative to brine saturated V_p. CO_2 flooding also increases V_s, typically 1%-2% and decreases density by 3%-5%. The sensitivity analysis by Sengupta and Mavko (2003) indicates that Gassmann's equations are most sensitive to the brine saturated V_p while the sensitivity to shear wave velocity and bulk density is much lower.

In comparison with the Reuss model or uniform saturation, the Voigt model or patchy saturation shows a more gradual decrease in P-wave velocity with CO_2 content and always leads to higher velocities. Therefore, it is crucial to define whether the patchy or the uniform model should be used to calculate CO_2 saturated greensand properties.

For analysis of amplitude variation with offset, the PP (R_{PP}) reflection coefficients were calculated. Zoeppritz's equations as given in Mavko et al., (2009) were used to calculate the reflection coefficient as a function of reflection angle ranging from 0^o to 30^o. Shale data for AVO curves were obtained from the studied Nini 1A well. The shale represents the cap-rock for the greensand. The V_p, V_s and density of brine bearing greensand sample 1A-142 were used as input to calculate the reflection coefficient. Data representing the CO_2 bearing state were calculated by using Gassmann's equations (Gassmann, 1951).

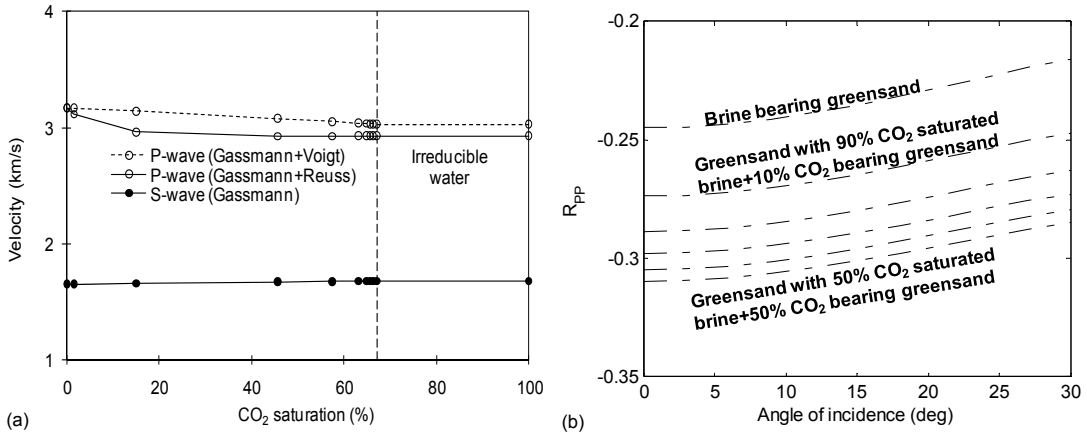

Figure 6.4. *(a) P-wave velocity and S-wave velocity of CO_2 bearing greensand samples as calculated from Gassmann's fluid substitution method, (b) PP refection coefficient (R_{pp}) versus incident angle of CO_2 bearing greensand.*

The corresponding AVO response shows a negative zero-offset reflectivity and a positive AVO gradient (Figure 6.4b). The AVO response of CO_2 saturated greensand is distinguishable both at zero and far offset. PP refection coefficients are monotonically decreasing with CO_2 saturation increase. Figure 6.4b demonstrates that the largest changes in the AVO responses occur when the first 10% CO_2 are injected into a brine saturated greensand. At higher CO_2 saturation levels, the change in AVO response is relatively small.

7. Conclusions

The total porosity of greensand measured by Archimedes method is close to Helium porosity, whereas NMR estimated porosity is lower the total porosity. The discrepancy between Archimedes porosity and NMR porosity may be due to the presence of iron bearing clay minerals in greensand.
Predicted permeability from NMR T_2 distribution by using Kozeny's equation agrees well with data when surface relaxivity is known. By using the traditional Timur-Coates model, predicting permeability works rather well if we optimize the constant to C=8.3. Permeability in greensand was found at two scales: permeability in large pores controlled by macro-porosity together with effective specific surface area and permeability in small pores controlled by micro-porosity together with specific surface measured by BET.
Predicted capillary pressure curves from NMR T_2 distribution overlay on measured capillary pressure curves for low permeability samples. The deviation between predicted capillary pressure curves from NMR T_2 distribution and measured capillary pressure curves for the high permeability samples is due to the contrasting relaxivity on the surface of quartz and glauconite.

Results of rock-physics modelling and thin section observations indicate that variations in elastic properties of greensand can be explained by two main diagenetic phases: silica cementation and berthierine cementation.
Initially, greensand is a mixture of quartz and glauconite grains; when weakly cemented, it has relatively low elastic moduli and can be modeled by the Hertz-Mindlin contact model for two types of grains.
Silica-cemented greensand has relatively high elastic moduli and can be modeled by an intermediate-stiff-sand or stiff-sand model.
Berthierine cement has a different growth pattern in the greensand formations, resulting in a soft-sand model and an intermediate-stiff-sand model.

New V_p-V_s relationships were derived by using data from the Paleocene greensand Nini oil field in the North Sea. A V_p-V_s relationship of greensand from the Iso-frame model was also derived and compared it with empirical V_p-V_s regressions from laboratory data as well as from well log data. Both simple empirical V_p-V_s regression of greensand and V_p-V_s relationship from modelling provide good prediction of V_s from the measured V_p.

AVO modelling indicates that an interface between shale and glauconitic greensand produces a stronger negative reflection coefficient than an interface between shale and quartzitic sandstone. Brine saturated greensand may have similar AVO response to oil saturated quartzitic sandstone. The observed difference in seismic response between the greensand and the quartzitic sandstone is due to the difference not only in mineralogy but also due to the compliant micro-porous glauconite grains.
AVO modelling also indicates that an interface between shale and weakly cemented greensand produces a stronger negative reflection coefficient than an interface between shale and cemented greensand. Cemented greensand with oil saturation can have similar AVO response to brine saturated weakly cemented greensand. The observed significant difference in the seismic response between the two types of greensands is due to a difference in greensand diagenesis.

Gassmann's equations are not enough to estimate the saturated elastic properties of greensand. This study shows that Biot's flow should occur only in large pores in greensand. Biot's flow should not occur in micro-pores. Differences of fluid flow in macro-pores and micro-pores pores are related to the high frequency squirt flow in greensand.

Laboratory results show that CO_2 injection has no major effect on porosity, electrical and elastic properties of greensand.
Klinkenberg permeability of greensand increased after CO_2 injection. An NMR T_2 distribution and NMR permeability modelling approach was tested to evaluate the effect on matrix permeability of CO_2 injection. It appears that permeability after CO_2 injection increased due to the increase of macro-pore size in the greensand. The increase of macro-pore size is probably due to migration of fine pore-filling minerals. The increased permeability is thus not caused by fracturing.
Rock physics modelling results show that the effect of CO_2 flooding alone decreases V_p by 2%-41%. CO_2 flooding also increases V_s, typically 1.9% and decreases density by 3%-5%. AVO modelling results shows that the largest change in the AVO response occurs when the first 10% CO_2 are injected into a brine saturated greensand.

8. Paper abstracts

Abstract from paper I

Nuclear magnetic resonance (NMR) is a useful tool in reservoir evaluation. The objective of this study is to predict petrophysical properties from NMR T_2 distributions. A series of laboratory experiments including core analysis, capillary pressure measurements, NMR T_2 measurements and image analysis were done on sixteen greensand samples from two formations in the Nini field of the North Sea. Hermod Formation is weakly cemented, whereas Ty Formation is characterized by microcrystalline quartz cement. The surface area measured by BET method and the NMR derived surface relaxivity are associated with the micro-porous glauconite grains. The effective specific surface area as calculated from Kozeny's equation and as derived from petrographic image analysis of Backscattered Electron Micrograph's (BSE), as well as the estimated effective surface relaxivity is associated with macro-pores. Permeability may be predicted from NMR by using Kozeny's equation when surface relaxivity is known. Capillary pressure drainage curves may be predicted from NMR T_2 distribution when pore size distribution within a sample is homogeneous.

Abstract from paper II

The relationship between V_p and V_s may be used to predict V_s where only V_p is known. V_p/V_s is also used to identify pore fluids from seismic data and amplitude variation with offset analysis. Theoretical, physical, as well as statistical empirical V_p-V_s relationships have been proposed for reservoir characterization when shear-wave data are not available. In published work, focus is primarily on the V_p-V_s relationship of quartzitic sandstone. In order to broaden the picture we present V_p-V_s relationships of greensand composed of quartz and glauconite by using data from the Paleocene greensand Nini oil field in the North Sea. A V_p-V_s relationship derived from modeling is compared with empirical V_p-V_s regressions from laboratory data as well as from well logging data. The quality of V_s prediction is quantified in terms of the rms error. We find that the V_p-V_s relationship derived from modeling works well for greensand shear-wave velocity prediction. We model seismic response of glauconitic greensand by using laboratory data from the Nini field with the goal of better understanding seismic response for this kind of rock. Our studies show that brine saturated glauconitic greensand may have similar seismic response to oil saturated

quartzitic sandstone and that strongly cemented greensand with oil saturation can have similar AVO response to brine saturated weakly cemented greensand.

Abstract from paper III

The objective of this study is to establish a rock-physics model of North Sea Paleogene greensand. The Hertz-Mindlin contact model is widely used to calculate elastic velocities of sandstone as well as to calculate the initial sand-pack modulus of the soft-sand, stiff-sand, and intermediate-stiff-sand models. When mixed minerals in rock are quite different e.g. mixtures of quartz and glauconite in greensand, the Hertz-Mindlin contact model of single type of grain may not be enough to predict elastic velocity. Our approach is first to develop a Hertz-Mindlin contact model for a mixture of quartz and glauconite. Next, we use this Hertz-Mindlin contact model of two types of grains as the initial modulus for a soft-sand model and a stiff-sand model. By using these rock-physics models, we examine the relationship between elastic modulus and porosity in laboratory and logging data and link rock-physics properties to greensand diagenesis. Calculated velocity for mixtures of quartz and glauconite from the Hertz-Mindlin contact model for two types of grains are higher than velocity calculated from the Hertz-Mindlin single mineral model using the effective mineral moduli predicted from the Hill's average. Results of rock-physics modeling and thin section observations indicate that variations in the elastic properties of greensand can be explained by two main diagenetic phases: silica cementation and berthierine cementation. These diagenetic phases dominate the elastic properties of greensand reservoir. Initially greensand is a mixture of mainly quartz and glauconite; when weakly cemented, it has relatively low elastic modulus and can be modeled by a Hertz-Mindlin contact model of two types of grains. Silica-cemented greensand has a relatively high elastic modulus and can be modeled by an intermediate-stiff-sand or a stiff-sand model. Berthierine cement has different growth patterns in different parts of the greensand, resulting in a soft-sand model and an intermediate-stiff-sand model.

Abstract from paper IV

The objective of this study is to investigate CO_2 injection effects on physical properties of greensand reservoir rocks from the North Sea Nini field. Greensands are sandstones composed of a mixture of clastic quartz grains and glauconite grains. A CO_2 flooding experiment was carried out by injecting supercritical CO_2 into brine saturated samples and subsequently flushing the CO_2

saturated samples with brine at reservoir conditions. Helium porosity, Klinkenberg permeability, and specific surface area by BET were measured on dry greensand samples before and after the CO_2 experiment. NMR T_2 distribution, electrical resistivity and ultrasonic P-and S-wave velocities were measured on brine saturated greensand samples before and after the CO_2 experiment. P-and S-wave velocities were also measured on dry samples. Our laboratory results indicate that CO_2 injection has no major effect on porosity, electrical and elastic properties of the greensand, whereas Klinkenberg permeability increased after CO_2 injection. An NMR permeability modeling approach was used to evaluate the effect on matrix permeability of CO_2 injection. It appears that permeability after CO_2 injection increased not due to fracturing but rather due to the increase of macro-pores in the greensand. The increase of macro-pore size is probably due to migration of fine pore-filling minerals. Rock physics modeling indicates that the presence of CO_2 in a greensand decreases V_p by 2%-41% relative to V_p of brine saturated greensand. CO_2 flooding would at the same time increase V_s, typically by 1%-2%, while decreasing density by 3%-5%. AVO modeling indicates that the largest change in the AVO response occurs when the first 10% CO_2 are injected into a brine saturated greensand.

9. References

Adam, L., Batzle, M. and Brevik, L., 2006. Gassmann's fluid substitution and shear modulus variability in carbonates at laboratory seismic and ultrasonic frequencies. *Geophysics*, **71**, no. 6, F173–F183.

Aki, K. and Richards, P.G., 1984. *Quantitative Seismology: Theory and Method*. San Francisco, CA: W.H. Freeman and Co.

Al-Mahrooqi S. H., Grattoni, C. A., Moss, A. K. and Jing, X. D., 2003. An investigation of the effect of wettability on NMR characteristics of sandstone rock and fluid systems. *Journal of Petroleum Science and Engineering,* **39**, 389-398.

Al-Mahrooqi, S. H., Grattoni, C. A., Muggeridge, A. H., Zimmerman, R. W. and Jing, X. D. , 2006. Pore-scale modeling of NMR relaxation for the characterization of wettability. *Journal of Petroleum Science and Engineering,* **52**, 172-186.

Assefa, S., McCann, C. and Sothcott, J., 2003. Velocities of compressional and shear waves in limestones. *Geophysical Prospecting*, **51**, 1–13.

Avseth, P., 2000. *Combining rock physics and sedimentlogy for seismic reservoir characterization of North Sea Turbidite systems*. Ph.D Thesis, Stanford University.

Avseth, P., Mukerji, T. and Mavko, G., 2005. *Quantitative seismic interpretation: applying rock physics tools to reduce interpretation risk*. Cambridge University Press.

Bachrach, R., Dvorkin, J. and Nur, A., 2000. Seismic velocities and Poisson's ratio of shallow unconsolidated sands. *Geophysics*, **65**, 559–564.

Backus, G.E., 1962. Long-wave elastic anisotropy produced by horizontal layering. *Journal of Geophysical Research*, **67**, 4427-4440.

Baechle, G. T., Eberli, G. P., Weger, R. J. and Massaferro, J. L., 2009. Changes in dynamic shear moduli of carbonate rocks with fluid substitution. *Geophysics*, **74**, 3, 135–147.

Batzle, M. and Wang, Z., 1992. Seismic properties of pore fluids. *Geophysics*, **57**, 1396-1408.

Batzle, M. L., Han, D. H. and Hofmann, R., 2006. Fluid mobility and frequency-dependent seismic velocity - Direct measurements. *Geophysics*, **71(1)**, 1–9.

Berryman, J. G., 1980. Confirmation of Biot's theory. *Applied Physics Letters*, **37**, 382–384.

Berryman, J.G., 1999. Origin of Gassmann's equations. *Geophysics*, **64**, 1627–1629.

Biot, M. A., 1956a. Theory of propagation of elastic waves in a fluid saturated porous solid. I. low-frequency range. *Journal of Acoustical Society of America*, **28**, 168-178.

Biot, M. A., 1956b. Theory of propagation of elastic waves in a fluid saturated porous solid. II. high-frequency range. *Journal of Acoustical Society of America*, **28**, 179-191.

Blangy, J.P., 1992. *Integrated seismic lithologic interpretation: The petrophysical basis*. Ph.D Thesis, Stanford University.

Borre, M., Lind, I. and Mortensen, J., 1997. Specific surface as a measure of burial diagenesis of chalk. *Zentralblatt fur Geologie und Palaontologie,* **1**, 1071–1078.

Brown, R. and Korringa, J., 1975. On the dependence of the elastic properties of a porous rock on the compressibility of the pore fluid. *Geophysics*, **40**, 608–616.

Brown, S., Bussod, G. and Hagin, P., 2007. AVO Monitoring of sequestration: A benchtop-modeling study. The Leading Edge, **26 (12)**, 1576-1583.

Budiansky, B., 1965. On the elastic moduli of some heterogeneous materials. *Journal of Mechanical Physics of Solids,* **13**, 223-227.

Cagatay, M. N., Saner, S., Al-Saiyed, I. and Carrigan W. J., 1996. Diagenesis of the Safaniya Sandstone Member (mid-Cretaceous) in Saudi Arabia. *Sedimentary Geology*, **105**, 221-239.

Carcione, J., Picotti, S., Gei, D. and Rossi, G., 2006. Physics and seismic modeling for monitoring CO_2 storage. *Pure and Applied Geophysics*, **163**, 175–207.

Castagna, J. P. and Smith, S. W., 1994. Comparison of AVO indicators: A modeling study. *Geophysics*, **59**, 1849-1855.

Castagna, J. P. and Swan, H. W., 1997. Principles of AVO cross-plotting. *The Leading Edge*, **16**, 337-342.

Castagna, J. P., 1993. Comparison of AVO indicators: A modeling study. *Geophysics*, **59**, 1849-1855.

Castagna, J., Batzle, M. and Eastwood, R., 1985. Relationships between compressional wave and shear-wave velocities in clastic silicate rocks. *Geophysics*, **50**, 571-581.

Castagna, J., Swan, H. W. and Foster, D. J., 1998. Framework for AVO gradient and intercept interpretation. *Geophysics*, **63**, 948-956.

Coates, G. R., Xiao, L. And Prammer, M., 1999. *NMR logging principles and applications*. Gulf Professional Publishing, Houston, Texas, 234.

Connolly, P., 1999. Elastic impedance. *The Leading Edge*, **18**, 438-452.

.

Coste, C., and Gilles, B., 1999. On the validity of Hertz contact law for granular material acoustics. *European Physical Journal*, **7**, 155–168.

Coyer, K. B., 1984. *Effects of stress, pore pressure, and pore fluids on bulk strain, velocity, and permeability in rocks*. Ph.D. thesis, Massachusetts Institute of Technology.

DeGennes, P., 1996. Static compression of a granular medium, the soft shell model. *Europhysics Letters*, **35**, 145–149.

Diaz, E., Prasad, M., Dvorkin, J. and Mavko, G., 2002. Effect of glauconite on the elastic properties, porosity, and permeability of reservoir rocks. AAPG Annual Meeting, March 10-13, Houston, Texas.

Diaz, E., Prasad, M., Mavko, G. and Dvorkin, J., 2003. Effect of glauconite on the elastic properties, porosity, and permeability of reservoir rocks. *The Leading Edge*, **22**, 42-45.

Digby, P. J., 1981. The effective elastic moduli of porous granular rocks. *Journal of Applied Mechanics*, **48**, 803–808.

Dodge, W. S., Shafer, J. L., Guzman-Garcia, A. G. and Noble, D. A., 1995. Core and Log NMR Measurements of an Iron-Rich, Glauconitic Sandstone Reservoir. *36th Annual Symposium of SPWLA*, Paris, France, June 26-29.

Dutta, T., 2009. *Integrating sequence stratigraphy and rock-physics to interpret seismic amplitudes and predict reservoir quality*. PhD Thesis, Stanford University.

Dvorkin, J. and Nur, A., 1996. Elasticity of high-porosity sandstones: Theory for two North Sea data sets. *Geophysics,* **61**, 1363-1370.

Dvorkin, J., Nolen-Hoeksema, R., and Nur, A., 1994. The squirt-flow mechanism: macroscopic description. *Geophysics,* **59**,428-438.

Fabricius, I. L., 2003. How burial diagenesis of chalk sediments controls sonic velocity and porosity. *AAPG Bulletin*, **87**, 1-24.

Fabricius, I. L., Høier, C., Japsen, P. and Korsbech, U., 2007. Modeling elastic properties of impure chalk from the South Arne Field, North Sea. *Geophysical Prospecting*, **55**, 487–506.

Fabricius, I.L., Bachle, G.T. and Eberli, G.P., 2010. Ealstic modulu of dry and water-saturated carbonates - Effect of depositional texture, porosity, permeability. *Geophysics*, **75**, 65-78.

Gassmann, F., 1951. Uber die elastizitat poroser medien. *Veirteljahrsschrift der Naturforschenden Gesellschaft*, **96**, 1–23.

Glover, P., Zadjali, I. and Frew, K., 2006. Permeability prediction from MICP and NMR data using an electrokinetic approach. *Geophysics,* **71**, 49-60.

Goddard, J. D., 1990. Nonlinear elasticity and pressure-dependent wave speeds in granular media: Proceedings of the Royal Society of London, Series A, Mathematical and Physical Sciences, **430**, 105–131.

Grattoni, C. A., Al-Mahrooqi, S. H., Moss, A. K., Muggeridge, A. H. and Jing, X. D., 2003. An improved technique for deriving drainage capillary pressure from NMR T2 distributions. *The International Symposium of the Society of Core Analysis,* **25,** 21-24 September, Pau, France.

Greenberg, M. and Castagna, J., 1992. Shear-wave velocity estimation in porous rocks: Theoretical formulation, preliminary verification and applications. *Geophysical Prospecting*, **40**, 195-209.

Gregory, A. R., 1976. Fluid saturation effects on dynamic elastic properties of sedimentary rocks. *Geophysics*, **4**, 895-921.

Hamada, G.M., Al-Blehed, M.S., and Al-Awad, M.N.J., 1999. Nuclear Magnetic Resonance Log Evaluation of Low-Resistivity Sandstone Reservoir. *Journal of Engineering Applied Science*, **46**, 951-970.

Hamada, G., Al-Blehed, M., Al-Awad, M. and Al-Saddique, M., 2001. Petrophysical evaluation of low-resistivity sandstone reservoirs with nuclear magnetic resonance log. *Journal of Petroleum Science and Engineering,* **29**, 129-138.

Han, D., 1986a. *Effects of porosity and clay content on acoustic properties of sandstones and unconsolidated sediments*. Ph.D.Thesis, Stanford University.

Han, D., Nur, A and Morgan, D., 1986b. Effect of porosity and clay content on wave velocities in sandstone. *Geophysics,* **51**, 2093-2107.

Hashin, Z. and Shtrikman, S., 1963. A variational approach to the theory of the elastic behaviour of multiphase materials. *Journal of Mechanics and Physics Solids*, **11**, 127-140.

Hertz, H., 1882. On the contact of rigid elastic solids and on hardness, Macmillan, paper 6.

Hidajat, I., Singh, M., Cooper, J. and Mohanty, K. K., 2002. Permeability of porous media from simulated NMR response. *Transport in Porous Media,* **48**, 225-247.

Hill, R., 1952. The elastic behavior of crystalline aggregate. *Proceeding of the Physical Society of London*, **65**, 349-354.

Hossain, Z., Fabricius, I. L. and Christensen, H. F., 2009. Elastic and nonelastic deformation of greensand. *The Leading Edge*, **28**, 260-262.

Hossain, Z., Mukerji, T. and Fabricius, I.L., 2010a. Vp-Vs relationship of glauconitic greensand. Extended abstracts, 72nd Annual EAGE conference, June 14-17, Barcelona, Spain.

Hossain, Z., Mukerji, T. and Fabricius, I.L., 2010b. Petrophysical properties of greensand as predicted from NMR measurements. Extended abstracts, 72nd Annual EAGE conference, June 14-17, Barcelona, Spain.

Hossain, Z., Mukerji, T., Dvorkin, J. and Fabricius, I.L., 2010c. Rock Physics model of glauconitic greensand from the North Sea. Extended abstract, 80th SEG annual conference, Denver October 17-25, Colorado, USA.

Hossain, Z., Mukerji, T., Dvorkin, J. and Fabricius, I.L., 2010d. Rock Physics model of glauconitic greensand from the North Sea. In: SRB Annual Meeting 23-25 June, 2010. Stanford Rock Physics & Borehole Geophysics Project. Annual Report Vol. 121, p. B1-B21, Stanford University, Stanford, CA.

Hossain, Z., Fabricius, I.L, Grattoni, A. C. and Solymar, M., 2011a. Petrophysical properties of greensand as predicted from NMR measurements. *Petroleum Geoscience* (in Press).

Hossain, Z. and Fabricius, I.L., 2011b. Effect of CO_2 injection on Physical properties of greensand. Extended abstracts, 73th Annual EAGE conference, May 23-26, Barcelona, Spain.

Hossain, Z., Mukerji, T. and Fabricius, I.L., 2011c. Vp-Vs relationship and AVO modeling of glauconitic greensand. *Geophysical Prospecting* (in Press).

Howard, J. J., Kenyon, W. E. and Straley, C., 1993. Proton magnetic resonance and pore size variations in reservoir sandstones. *SPE Formation Evaluation,* **1**, 194-200.

Jenkins, J., D. Johnson, L. La Ragione, and Makse, H., 2005. Fluctuations and the effective moduli of an isotropic, random aggregate of identical, frictionless spheres. *Journal of the Mechanics and Physics of Solids*, **53**, 197–225.

Johnson, K.L., 1985., *Contact Mechanics*. Cambridge University Press.

Jørstad, A., Mukerji, T. and Mavko, G., 1999. Model-based shear-wave velocity estimation versus empirical regressions. *Geophysical Prospecting*, **47**, 785-797.

Kazemeini, S.H., Juhlin, C. and Fomel, S., 2010. Monitoring CO_2 response on surface seismic data; a rock physics and seismic modeling feasibility study at the CO_2 sequestration site, Ketzin, Germany. *Journal of Applied Geophysics*, **71**, 109–124.

Kenyon, B., Kleinberg, R., Straley, C. and Morriss, C., 1995. Nuclear Magnetic Resonance Imaging—Technology for the 21st Century. *Oilfield Review,* **7**, 19–30.

Kenyon, W. E., 1997. Petrophysical principles of applications of NMR logging. *The Log Analyst,* **38**, 21-43.

Kewan, W. and Ning, L., 2008. Numerical simulation of rock pore-throat structure effects on NMR T_2 distribution. *Applied Geophysics,* **5**, 86-91.

Kleinberg, R., 1996. Utility of NMR T2 distributions, connection with capillary pressure, clay effect, and determination of the surface relaxivity parameter ρ_2. *Magnetic resonance imaging,* **14**, 761-767.

Kozeny, J., 1927. Ueber kapillare Leitung des Wassers im Boden. *Sitzungsber.Akad.Wiss.Wien,* **136**, 271-306.

Krief, M., Garat, J., Stellingwerff, J. and Ventre, J., 1990. A petrophysical interpretation using the velocities of P and S waves (full-waveform sonic). *Log Analyst*, **31**, 355-369.

Kuster, G.T. and Toksoz, M.N., 1974. Velocity and attenuation of seismic waves in two phase media. *Geophysics,* **39**, 587-618.

Lei, X. and Xueb, Z., 2009. Ultrasonic velocity and attenuation during CO_2 injection into water-saturated porous sandstone: Measurements using difference seismic tomography. *Physics of the Earth and Planetary Interiors*, **176**, 224-234.

Li, Y., Downton, J. and Xu, Y., 2007. Practical aspects of AVO modeling. *The Leading Edge*, **26**, 295-311

Ma, J. and Morozov, I., 2010. AVO modeling of pressure-saturation effect in Weyburn CO_2 sequestration. *The Leading Edge*, **29**, 178-183.

Makse, A., Gland, N., Johnson, D. and Schwartz, L., 2004. Granular packings: Nonlinear elasticity, sound propagation, and collective relaxation dynamics. *Physics Review*, **70**, 061302.

Marion, D., 1990. *Acoustical, mechanical and transport properties of sediments and granular materials*. Ph.D.Thesis, Stanford University.

Marion, D., Nur, A., Yin, H. and Han, D., 1992. Compresional velocity and porosity in sand-clay mixture. *Geophysics,* **57**. 554-563.

Marschall, D., Gardner, J. S., Mardon, D. and Coates, G. R., 1995. Method for correlating NMR relaxometry and mercury injection data. *Proceeding of the 1995 International Symposium of Society of core Analysts,* papers 9511.

Mavko, G. and Jizba, D., 1991. Estimating grain-scale fluid effects on velocity dispersion in rocks. *Geophysics*, **56**, 1940-1949.

Mavko, G., Mukerji, T. and Dvorkin, J., 2009. The Rock Physics Handbook. Tools for Seismic Analysis of Porous Media. Cambridge University press. Second Edition.

McKenna, J.J., Gurevich, B., Urosevic, M. and Evans, B.J., 2003. Rock physics-application to geological storage of CO_2. APPEA Journal 43, 567–576.

Milholland, P., Manghnani, M.H., Schlanger, S.O. and Sutton, G.H., 1980. Geo-acoustic modelling of deep-sea carbonates sediments. *Journal of Acoustical Society of America*, **59**, 2368-2375.

Mindlin, R. D., 1949. Compliance of elastic bodies in contact. *Journal of Applied Mechanics*, **16**, 259–268.

Mindlin, R. D., Mason, W. P., Osmer, I. F. and Deresiewicz, H., 1951. Effects of an oscillating tangential force on the contact surfaces of elastic spheres. Proceedings of the First U. S. *National Congress of Applied Mechanics*, 203–208.

Morgan, J.T. and Gordon, D.T., 1970. Influence of pore geometry on water-oil relative permeability. *Journal of Petroleum Technology*, **22**, 1199-1208.

Mortensen, J., Engstrøm, F. and Lind, I., 1998. The relation among porosity, permeability, and specific surface of chalk from the Gorm field, Danish North Sea. *SPE Reservoir Evaluation and Engineering,* **1**, 245-251.

Mukerji, T., Berryman, J.G., Mavko, G. and Berge, P.A., 1995. Differential effective medium modeling of rock elastic moduli with critical porosity constraints. *Geophysics Research Letter,* **22**, 555-558.

Mukerji, T., Jorstad, A., Avseth, P., Mavko, G., and Granli, J. R., 2001. Mapping lithofacies and pore fluid probabilities in a North Sea reservoir: Seismic inversions and statistical rock physics. *Geophysics*, **66**, 988-1001.

Murphy, W. F., 1982. *Effects of microstructure and pore fluids on the acoustic properties of granular sedimentary materials*. Ph.D. Thesis, Stanford University.

Murphy, W. F., 1984. Acoustic measures of partial gas saturation in tight sandstones. *Journal of Geophysical Research*, **89(13)**, 549-11,559.

Norris, A. N., and Johnson, D. L., 1997. Non-linear elasticity of granular media. *Journal of Applied Mechanics*, **64**, 39–49.

Pickett, G.R., 1963. Acoustic character logs and their applications in formation evaluation. *Journal of Petroleum Technology*, **15**, 650-667.

Ranganathan, V. and Tye, R. S., 1986. Petrography, diagenesis, and facies controls on porosity in Shannon Sandstone, Hartzog Draw Field, Wyoming. *AAPG Bulletin,* **70**, 56-69.

Raymer, L.L., Hunt, E.R. and Gardner, J.S., 1980. An improved sonic transit time-to-porosity transform. Trans. Society of Professional Well Log Analysts, 21st Annual Logging Symposium, Paper P.

Reuss, A., 1929. Berechnung der Fliessgrenzen von Mischkristallen auf Grund der Plastizitatsbedingung fur Einkristalle, *Zeitschrift fur Angewandte Mathematik und Mechanik,* **9**,49-58.

Riepe, L., 1998. Specific internal surface: the "forgotten?" petrophysical measurement! *Proceeding of the 1998 International Symposium of Society of core Analysts,* papers 9540.

Røgen, B. and Fabricius, I.L., 2002. Influence of clay and silica on permeability and capillary entry pressure of chalk reservoir in the North Sea. *Petroleum Geopscience*, **8**, 287-293.

Røgen, B., Fabricius, I. L., Japsen, P. Høier, C., Mavko, G. and Pedersen, J. M., 2005. Ultrasonic velocities of North Sea chalk samples—Influence of porosity, fluid content and texture. *Geophysical Prospecting*, **53**, 481–496.

Rueslåtten, H., Eidesmo, T., Lehne, K. A. and Relling, O. M., 1998a. The use of NMR spectroscopy to validate NMR logs from deeply buried reservoir sandstones. *Journal of Petroleum Science and Engineering,* **19**, 33-44.

Rueslåtten, H., Eidsemo, T. and Slot-Petersen, C., 1998b. NMR studies of iron-rich sandstone oil reservoir. *Proceeding of the 1998 International Symposium of Society of core Analysts,* papers 9821.

Schiøler, P., Andsbjerg, J., Clausen, O. R., Dam, G., Dybkjær, K., Hamberg, L., Heilmann-Clausen, C., Johannessen, E. P., Kristensen, L. E. and Prince, I., 2007. Lithostratigraphy of the Paleocene: Lower Neogene succession of the Danish North Sea. *Geological Survey of Denmark and Greenland Bulletin*, **12**, 77.

Sengupta, M.and Mavko, G., 2003. Impact of flow-simulation parameters on saturation scales and seismic velocity. *Geophysics*, **68**, 1267–1280.

Shuey, R.T., 1985. A simplification of the Zeopprittz equation. *Geophysics,* **50**, 609-614.

Siggins A. F., 2006. Velocity-effective stress of CO_2-saturated sandstone. *Exploration Geophysics,* **37**, 60-66.

Slot-Petersen, C., Eidsemo, T., White, J. and Rueslatten, H. G., 1998. NMR formation evaluation application in a complex low resistivity hydrocarbon reservoir. *Transactions of the SPWLA 39th Annual Logging Symposium*, Paper 1998-TT .

Solymar, M., 2002. Influence *of composition and pore geometry on immiscible fluid flow through greensand*. Ph.D.Thesis, Chalmers University of Technology.

Solymar, M., Fabricus, I.L. and Middleton, M.F., 2003. Flow characterization of glauconitic sandstones by interated Dynamic Neutron Radiagraphy and image analysis of backscattered electron micrographs. *Petroleum Geoscience*, **9**, 175-183.

Spencer, J.W., 1981. Stress relaxations at low frequencies in fluid-saturated rocks: Attenuation and modulus dispersion. *Journal of Geophysical Research*, **86**, 1803–1812.

Stokkendal, J., Friis, H., Svendsen, J. B., Poulsen, M. L. K. and Hamberg, L., 2009. Predictive permeability variations in a Hermod sand reservoir, Stine Segments, Siri Field, Danish North Sea. *Marine and Petroleum Geology***, 26**, 397-415.

Straley, C., Roosini, D., Vinegar, H., Tutunjian, P. and Morriss, C., 1997. Core analysis by low-field NMR. *The Log Analyst,* **38**, 84-94.

Tilley, B. J. and Longstaffe, F. J., 1984. Controls on hydrocarbon accumulation in glauconitic sandstone, Suffield heavy oil sands, southern Alberta. *AAPG Bulletin***, 68**, 1004-1023.

Tsuneyama, F., 2005. *Quantitative detection of fluid distribution using time-lapse seismic*. Ph.D Thesis, Stanford University.

Vernik, L., Fisher, D., and Bahret, S., 2002. Estimation of net-to-gross from P and S impedance in deepwater turbidites. *The Leading Edge*, **21**, 380-387.

Voigt, W., 1910. *Lehrbuch der Kirstallphysik*: B. G. Teubner-Verlag.

Volokitin, Y., Looyestijn, W. J., Slijkerman, W. F. J. and Hofman, J. P., 1999. A Practical Approach to Obtain 1st Drainage Capillary Pressure Curves From NMR Core and Log Data. *The International Symposium of the Society of Core Analysts,* **24**, 1–4.

Walton, K., 1987. The effective elastic moduli of a random pack of spheres. *Journal of the Mechanics and Physics of Solids*, **35**, 213–226.

Wang, Z. Michael E. C., and Robert T. L., 1998, Seismic monitoring of a CO_2 flood in carbonate reservoir: A rock physics study. *Geophysics*, 63, 1604-1617.

Wang, Z., 2000. Dynamic versus static properties of reservoir rocks, in seismic and acoustic velocities in reservoir rocks. *SEG Geophysics Reprint Series,* **19**, 531-539.

Wang, Z., 2001. Fundamentals of seismic rock physics. *Geophysics*, **66**, 398–412

Wang, Z., and Nur, A., 1988. Velocity dispersion and the "local flow" mechanism in rocks: 58th Annual International Meeting, SEG, Expanded Abstracts, 548–550.

Wang, Z., and Nur, A., 1992, Seismic and acoustic velocities in reservoir rocks. *SEG Geophysics Reprint Series*, **10**.

Winkler, K. W., 1983. Frequency dependent ultrasonic properties of high-porosity sandstone. *Journal of Geophysical Research*, **88**, 9493-9499.

Winkler, K. W., 1985. Dispersion analysis of velocity and attenuation in Berea sandstone. *Journal of Geophysical Research*, **90**, 6793-6800.

Winkler, K. W., 1986. Estimates of velocity dispersion between seismic and ultrasonic frequencies. *Geophysics*, **51**, 183-189.

Winn, R. D., 1994. Shelf Sheet-Sand Reservoir of the Lower Cretaceous Greensand, North Celtic Sea Basin, Offshore Ireland. *AAPG Bulletin*, **78**, 1775-1789.

Wyllie, M., Gardner, G., and Gregory, A., 1963. Studies of elastic wave attenuation in porous media. *Geophysics*, **27**, 569-589.

Wyllie, M., Gardner, R. J. and Gregory, A. R., 1962. Studies of elastic wave attenuation in porous media, *Geophysics*, **2,** 569-589.

Wyllie, M., Gregory, A., and Gardner, G., 1956. Elastic wave velocities in heterogeneous and porous media. *Geophysics*, **21**, 41-70.

Wyllie, M., Gregory, A., and Gardner, G., 1958. An experimental investigation of factors affecting elastic wave velocities in porous media. *Geophysics*, **23**, 459-493.

Xie, R. H., Xiao, L. Z., Wang, Z. D. and Dunn, K. J., 2008. The influence factors of NMR logging porosity in complex fluid reservoir. *Science in China Series D: Earth Sciences*, **51**, 212-217.
Xu, S. and White, R. E., 1995. A new velocity model for clay-sand mixtures. *Geophysical Prospecting*, **43**, 91-118.

Xu, S. and White, R. E., 1996. A physical model for shear-wave velocity prediction. *Geophysical Prospecting*, **44**, 687-718.
Xue, Z., Ohsumi, T., 2004. Seismic wave monitoring of CO_2 migration in water-saturated porous sandstone. *Exploration Geophysics*, **35**, 25–32.

Zimmer, M., 2003. *Seismic velocities in unconsolidated sands: Measurements of pressure, sorting, and compaction effects*. Ph.D. Thesis, Stanford University.

Zimmerman, R.W., 1991. *Compressibility of Sandstones,* Elsevier, New York, 173 pp.

10. Papers

I. **Hossain, Z.**, Fabricius, I.L., Grattoni, A. C. and Solymar, M. (2011): Petrophysical properties of greensand as predicted from NMR measurements. *Petroleum Geoscience,* vol 17, No. 2, pp 111-125.

II. **Hossain, Z.**, Fabricius, I.L., Mukerji, T. and Dvorkin, J. (2011): Rock Physics model of glauconitic greensand from the North Sea. *Geophysics* (submitted revised version).

In: SRB Annual Meeting 23-25 June, 2010. Stanford Rock Physics & Borehole Geophysics Project. Annual Report Vol. 121, p. B1-B21, Stanford University, Stanford, CA.

III. **Hossain, Z.**, Fabricius, I.L. and Mukerji, T. (2011): V_p-V_s relationship and AVO modeling for glauconite bearing sandstone. *Geophysical Prospecting* (in press).

IV. **Hossain, Z.** and Fabricius, I.L. (2011). Effect of CO_2 injection of physical properties of greensand. *Journal of Petroleum science and Engineering* (submitted).

V. **Hossain, Z.**, and Mukerji, T (2011). Statistical rock physics and Monte Carlo simulation of seismic attributes for greensand (Accepted for EAGE annual meeting, Vienna, May 23-26, 2011).

VI. **Hossain, Z.**, Fabricius, I.L. and Christensen, H.F. (2009): Elastic and non-elastic deformation of greensand. *The Leading Edge*, Volume 28, Issue 1, pp.86-88.

The papers are not included in this www-version, but can be obtained from the library at DTU Environment. Contact library@env.dtu.dk or Department of Environmental Engineering, Technical University of Denmark, Miljoevej, Building 113, DK-2000 Kgs. Lyngby, Denmark.

The Department of Environmental Engineering (DTU Environment) conducts science-based engineering research within four themes:
Water Resource Engineering, Urban Water Engineering,
Residual Resource Engineering and Environmental Chemistry & Microbiology.
Each theme hosts two to four research groups.

The department dates back to 1865, when Ludvig August Colding, the founder of the department, gave the first lecture on sanitary engineering as response to the cholera epidemics in Copenhagen in the late 1800s.

DTU Environment
Department of Environmental Engineering
Technical University of Denmark

Miljoevej, building 113
DK-2800 Kgs. Lyngby
Denmark

Phone: +45 4525 1600
Fax: +45 4593 2850
e-mail: reception@env.dtu.dk
www.env.dtu.dk

ISBN 978-87-92654-36-6